Inhalable Perfluorocarbon Nanocapsules for RNA-based Immunotherapeutic Treatment of Lung Metastases

*Kasturi Siddhanta, Atefehsadat Monirvaghefi, Aditya Sundar, Braeden R. Pinkerton, Neha Kumari, Ling Ding, C. J. Woslager, Marjina Akter Kalpana, Chinmay M. Jogdeo, Ashley R. Ravnholdt, Jill A. Poole, Joshua L. Santarpia, James E. Talmadge, and David Oupický**

K. Siddhanta, A. Monirvaghefi, B. Pinkerton, N. Kumari, L. Ding, C. M. Jogdeo, D. Oupický
Department of Pharmaceutical Sciences, College of Pharmacy, University of Nebraska Medical Center, Omaha, NE 68198, USA
*E-mail: david.oupicky@unmc.edu

K. Siddhanta, B.R. Pinkerton, N. Kumari, D. Oupický
Center for Drug Delivery and Nanomedicine, University of Nebraska Medical Center, Omaha, Nebraska 68198, USA

A. Sundar
Materials Science Division, Argonne National Laboratory, 9700 S. Cass Avenue, Lemont, IL 60439, USA

L. Ding
Clinical Pharmacology Laboratory, Department of Pharmacy Practice and Science, University of Nebraska Medical Center, Omaha, NE 68198, USA

C. J. Woslager, Ashley R. Ravnholdt, J. L. Santarpia, J. E. Talmadge
Department of Pathology, Microbiology and Immunology, University of Nebraska Medical Center, Omaha, NE, 68198, USA

M. A. Kalpana
Department of Genetics, Cell Biology and Anatomy, University of Nebraska Medical Center, Omaha, NE, 68198, USA

J. L. Santarpia
Global Center for Health Security, University of Nebraska Medical Center, Omaha, NE, 68198, USA.

J. A. Poole
Division of Allergy & Immunology, University of Nebraska Medical Center, Omaha, Nebraska, USA

D. Oupický

Fred & Pamela Buffett Cancer Center, University of Nebraska Medical Center, Omaha, Nebraska 68198, USA

Funding: Funds from University of Nebraska Medical Center and grants P30 GM127200, R01 CA235863, R01 DK120533, and R01 DK124095

Keywords: perfluorocarbon, RNAi delivery, inhalable genetic medicine, cancer immunotherapy

While chemotherapy and pulmonary metastasectomy are leading clinical treatments for lung metastases, their effectiveness is limited by high recurrence rates and systemic side effects. Preclinical treatments have shown the promise of inhalation-based RNA therapy as a viable approach that can circumvent first pass metabolism and reduce systemic exposure. Here, we develop an inhalable perfluorocarbon nanocapsule for the targeted delivery of RNA interference therapeutics to lung metastases. Administering the aerosolized nanocapsules results in uptake by lung epithelial and tumor cells, extended retention times over 48 h, minimal inflammatory response, negligible clearance by pulmonary immune cells, and minimal accumulation in other organs. Compared to standard chemotherapy, our treatment not only drastically reduces metastatic tumor burden, but also demonstrates enhanced anti-tumor immunity in the tumor microenvironment resulting in nearly doubled lifespans after just three doses over two weeks. Finally, molecular dynamics simulations to study agglomeration tendency indicate that excipients such as stearate and vitamin E bind strongly with the nanocapsule and can potentially inhibit agglomeration, thereby enhancing the shelf-life of these formulations. In summary, this study demonstrates the promise of inhalable perfluorocarbon-based delivery systems as a non-invasive, biocompatible, and effective lung tumor-targeting platform that can overcome the challenges of current treatments.

1. Introduction

Lung metastases affect nearly one-third of all cancer patients and pose a significant clinical challenge, particularly in malignancies like sarcomas, colorectal, lung, breast, and renal cancer [1]. In breast cancer, lung metastases occur in about 27% of metastatic cases [2] and drastically impact disease outcomes, with overall mean survival of around 32 months following pulmonary metastasectomy [3]. Lung metastases are often aggressive, exhibit high recurrence rates, and are influenced by hypoxic tumor microenvironment, which can promote cancer stem cell-like properties associated with chemoresistance and increased metastatic potential [4]. Chemotherapy and pulmonary metastasectomy remain treatment options for select patients with limited lung metastases [5], offering potential for local control and improved survival [6]. However, these options offer limited curative potential, as negative hormone receptor status, incomplete resection, early recurrence, and the presence of multiple metastases markedly worsen outcomes and patient prognosis [6]. Thus, there is a critical need to develop novel approaches to treat lung metastasis to improve survival outcomes.

Pulmonary delivery of therapeutic RNA via inhalation offers a promising strategy for treating lung diseases, including lung metastases [7]. This approach provides direct access to the airways, enabling localized treatment and high drug concentrations at the site of action [8]. Consequently, this method facilitates rapid clinical responses while minimizing systemic exposure and associated systemic adverse effects [9-10]. By circumventing first-pass metabolism, inhaled therapeutics may achieve equivalent or greater efficacy compared to systemic administration at a fraction of the dose [11]. Furthermore, inhalation is a non-invasive route of administration, enhancing patient comfort and compliance [7, 9-10, 12]. Recent advances in lipid nanoparticle (LNP) and aerosolization technology have further propelled the potential of inhaled RNA therapeutics to effectively target and treat lung metastases [13-15]. Furthermore, the development of novel microfluidic platforms has enabled shear-free generation of LNP aerosols, preserving their structural integrity and improving delivery efficiency [16]. Despite the pre-clinical advances in inhalable pulmonary delivery systems, clinical translation remains in early stages due to challenges such as rapid immune clearance and observed toxicity [12, 17].

Designing successful pulmonary delivery systems requires careful optimization of particle properties, including size, morphology, surface characteristics, cell targeting and evasion of host defenses [11]. The deposition of inhaled particles in the respiratory tract is governed by the aerodynamic diameter of the aerosol particles which represents the diameter of a unit-density

spherical particle (1 g/cm³) that has the same settling velocity in air as the particle being measured [18-19]. Particles of 1-5 μm being optimal for lower airway targeting [19], while particles > 6 μm deposit in upper airways and those < 0.5 μm risk being exhaled [20-21]. The presence of lung tumors can obstruct the airways and divert airflow patterns, potentially hindering microparticle delivery to the tumor site [19]. Simulations indicate that particles accumulate increasingly at tumor sites until the tumor growth obstructs roughly 50% of the airway passage, after which particle deposition diminishes as blockage becomes more severe [22]. Therefore, to effectively target lung tumors, both the nanoparticle formulation and its aerosolized form must be optimized. The aerosol delivery parameters, including particle aerodynamic diameter, density, shape, and dispersibility, govern respiratory tract deposition patterns and determine whether particles reach the targeted lung regions. Meanwhile, the nanoparticle formulation itself must facilitate retention within the targeted lung tissue, enhance permeability into tumors, and evade clearance mechanisms like mucociliary transport and phagocytosis [23]. This can be achieved through various particle engineering strategies. For dry powder formulations, creating inhalable aggregates, where nanoparticles are co-formulated with other agents to form particles with aerodynamic diameters of 1-5 μm, helps overcome the tendency of individual nanoparticles <500 nm to agglomerate due to strong cohesive forces and poor dispersibility. For liquid formulations, strategies include nebulization of nanoparticle suspensions with appropriate surfactants to maintain stability and prevent aggregation during aerosolization. Regardless of formulation type, other approaches include surface modification by surfactant coating, active targeting using tumor-specific ligands, reducing phagocytic clearance using large porous particles, or using anti-fibrotic agents that can decrease tumor interstitial fibrosis and improve the intratumoral distribution of nanoparticles [19].

Perfluorocarbons (PFCs) offer multiple benefits for pulmonary RNA therapy through several biophysical and biological mechanisms that enhance the delivery, distribution, and overall transfection efficiency. Their unique properties, including high density and low surface tension at PFC-air interfaces enable them to readily spread and form thin films over the hydrophobic components of the lung surfactant, thus facilitating improved pulmonary distribution of delivery vectors by potentially penetrating mucus and ensuring uniform spread across the alveolar surface [24-26]. For instance, combined pulmonary delivery of perflubron and adenoviral vectors resulted in a 2-3-fold increase in total lung reporter gene expression, along with improved distribution throughout the lung and increased activity in distal lung tissue [27-28]. Importantly, PFCs do not alter the surface tension properties of the pulmonary surfactant

because of their inert nature, thereby providing a stable environment for gas exchange [29]. PFCs can also enhance lung retention by mitigating mucociliary clearance and limiting the rapid washout often seen with conventional aerosolized formulations due to the particles being inert [24, 30-32]. This prolonged retention time provides an extended window for cellular uptake and therapeutic activity, which is particularly advantageous for RNA interference (RNAi) therapeutics where sufficient intracellular accumulation is required for sustained RNA interference effects. Furthermore, the high oxygen solubility of PFCs can enhance various cancer treatments, including gene therapy, by improving tumor oxygenation and overcoming hypoxia-associated resistance [33-34]. Certain PFC formulations can also potentially modulate immune responses to reduce the inflammatory response upon particle administration to the lungs [35]. For instance, PFC administration decreased the release of leukotriene B4 and interleukin 6 in the bronchoalveolar lavage fluid of surfactant-depleted newborn pigs, playing a protective role against acute pulmonary inflammation [36]. This potential modulatory effect of PFCs on acute inflammatory responses may be determined by the extent of PFC partitioning into the lipid bilayers of cellular membranes [37]. Also, studies demonstrate that PFCs can block tumor necrosis factor-α-induced interleukin 8 release from alveolar epithelial cells and preventing neutrophil-mediated injury. This protection is achieved by PFCs acting as a mechanical barrier that prevents immune cells from penetrating their thin layers [38-40].

While PFCs hold great promise for pulmonary delivery applications, they present challenges due to the difficulty in formulating thermodynamically stable formulations suitable for clinical use [41]. PFCs spread well on hydrophobic surfaces , however, they present formulation challenges due to the extremely high interfacial tension between PFCs and aqueous media, making it difficult to create stable PFC-water nanointerfaces without specialized surfactants. To address this, we proposed an inhalable RNA nanocapsule delivery platform utilizing PFCs surface-coated with an in-house developed amphiphilic polymer surfactant for enhanced stability and tumor targeting. Our design leverages PFCs' unique properties to improve RNA delivery to tumors while maintaining stability during aerosolization and post-deposition. This PFC-based delivery system was engineered to facilitate the delivery of therapeutic miRNA that could reprogram the tumor microenvironment, thereby potentially increasing sensitivity to immune checkpoint blockade therapies through targeted modulation of immune responses in the tumor. In this study, we comprehensively characterized the nanocapsules for aerosolized delivery including their aerodynamic properties, evaluated their differential cellular uptake across various pulmonary cell types as well as pulmonary metastatic cells, assessed their safety

profile, biodistribution, tumor retention, immune cell mediated clearance, and therapeutic efficacy through aerosolized delivery of therapeutic miRNA in mouse models of lung metastatic breast cancer. We also conducted a survival analysis and detailed immunomodulation studies to investigate the potential of our platform to enhance anti-tumor immune response within the tumor microenvironment and address existing limitations of conventional chemotherapeutic treatments (Figure 1). Lastly, we also conducted molecular dynamics simulations to study the nanoparticles and model the impact of various excipients on their agglomeration tendency.

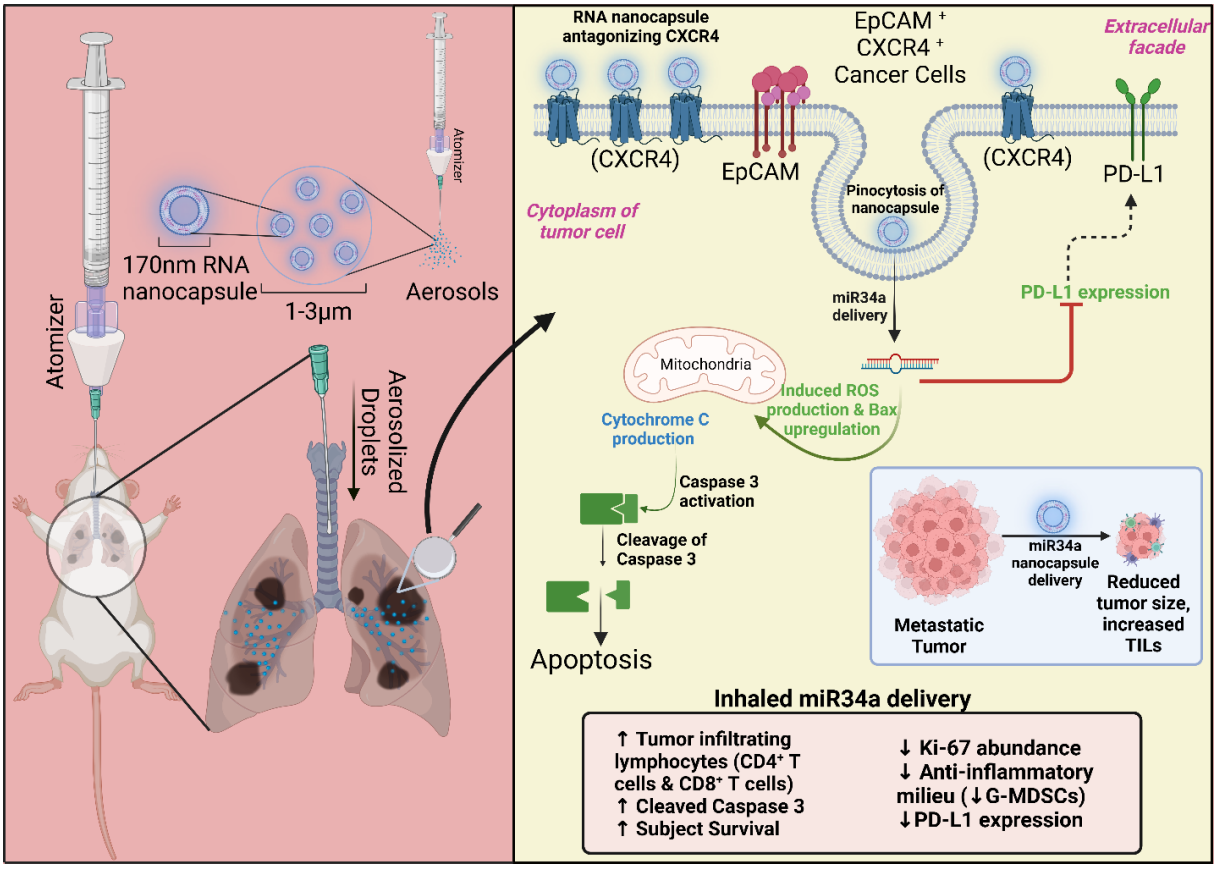

Figure 1. Schematic illustration of the mechanism of action of PFC-based RNA nanocapsules in the treatment of lung metastases. RNA nanocapsules encapsulating miR34a are formulated by mixing fixed ratios of nanoemulsion to miRNA. RNA nanocapsules are administered by microsprayer aerosolizer, intratracheally. CXCR4 is overexpressed on malignant lung metastatic cells which provides passive homing of the RNA nanocapsules to the sites of metastasis, aiding in the uptake and retention of RNA nanocapsules. Following endocytosis, the miR34a released from RNA nanocapsules suppresses PD-L1 expression and enhances cleavage of Caspase 3, thereby inducing apoptosis and alleviating metastatic tumors. miR34a nanocapsules exhibit multiple therapeutically beneficial mechanisms: we show that they induce apoptosis through increased levels of cleaved Caspase 3 and reduced Ki-67 abundance. Additionally, miR34a nanocapsules reduce the immunosuppressive milieu by reducing PD-L1 expression, allowing for increased tumor lymphocyte infiltration and reduction in granulocytic myeloid derived suppressor cells. *Created with Biorender.com.*

2. Results and Discussion

Our previous work established poly(amidoamine) derived from a CXCR4 antagonist AMD3100 (PAMD) as an effective dual-function carrier to simultaneously inhibit CXCR4/SDF-1 signaling achieving enhanced delivery of therapeutic nucleic acids [42-44]. In this project, amphiphilic derivative of PAMD reported in [45-46], was used as an emulsifier to prepare oil-in-water PFOB nanoemulsions [47-48].

2.1 Synthesis and characterization of aerosolized PAMD-C@PFOB nanoemulsion

PAMD was synthesized with the weight-average molar mass (M_w) of 13.9 kg/mol and dispersity ($Đ$) of 1.1 (Table S1). The structure was confirmed by ^{1}H-NMR (Figure S1). PAMD-C was then synthesized by reacting to the secondary amine groups in PAMD with cholesteryl chloroformate (Scheme S1). The cholesterol content of 17 wt % was determined from ^{1}H-NMR integral intensity of the cholesterol methyl group at 0.65 ppm (peak b) and the aromatic phenylene signals (peak a) from AMD3100 at 7.1-7.5 ppm (Figure S2). Using the known molar mass of the PAMD and cholesterol content, we calculated the final molecular weight of the PAMD-C copolymer to be 16.9 kg/mol (Table S1).

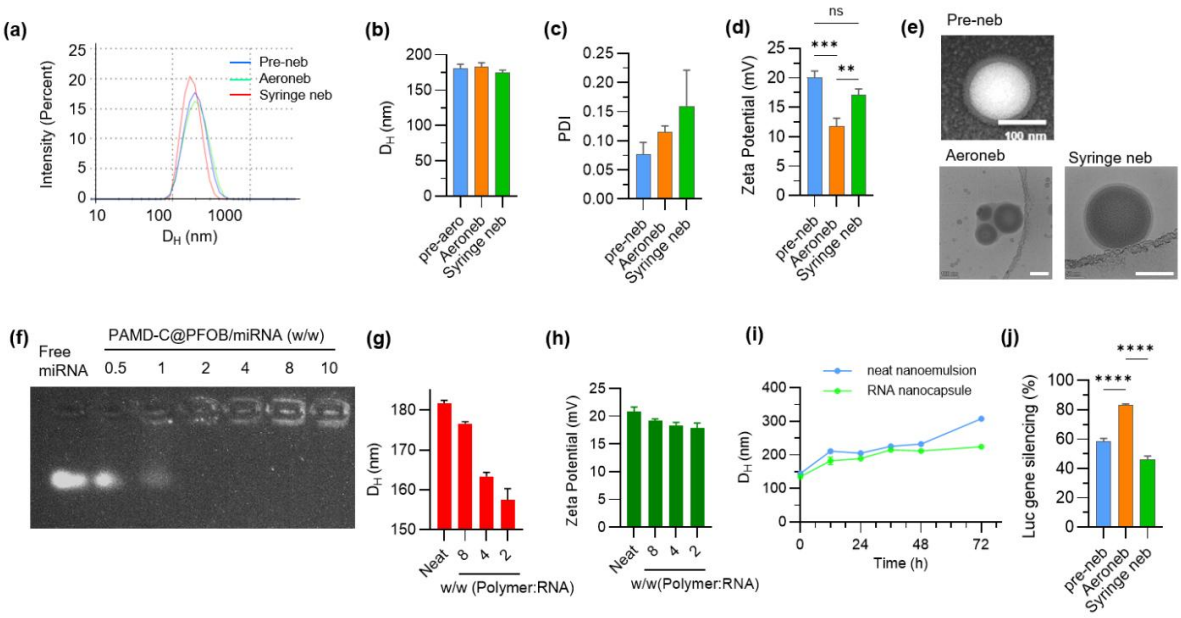

Figure 2. Formulation and characterization of PAMD-C@PFOB nanoemulsion and PAMD-C@PFOB/miRNA nanocapsules. a) Size distribution of nanoemulsion pre- and post-aerosolization. b) Mean hydrodynamic size, c) mean polydisperisty index (PDI), and d) mean zeta potential of nanoemulsions pre- and post-aerosolization by DLS. e) Representative TEM image of the RNA nanocapsule before aerosolization and representative CryoTEM images of the aerosolized RNA nanocapsules (w/w 4), scale bar = 100 nm in all three images, f) miRNA condensing ability of PAMD-C@PFOB nanoemulsion by agarose gel retardation assay. g) Mean hydrodynamic particle size and h) mean zeta potential of the RNA nanocapsules at different w/w ratios by DLS. i) Colloidal stability of the nanoemulsions and the RNA nanocapsules at room temperature for three days. j) In vitro luciferase

gene silencing evaluation of PAMD-C@PFOB/siLuc nanocapsules in 4T1.Luc cells pre- and post-aerosolization. The mean values and SD bars in (b-d), (g-j) are obtained using n = 3 replicates each. **** $p < 0.0001$, *** $p < 0.001$, ** $p < 0.01$.

PAMD-C@PFOB oil-in-water nanoemulsions were prepared using a one-step ultrasonication method [49] using 1% v/v PFOB and 2 mg/mL PAMD-C. The nanoemulsions were aerosolized using two methods: (i) a vibrating mesh nebulizer (AeronebPro), denoted as Aeroneb and (ii) and a syringe microsprayer aerosolizer, denoted here as Syringe neb. The hydrodynamic diameter (D_H) of the pre-nebulized nanoemulsions showed log-normal distributions (**Figure 2a**). The z- average value of the distribution for D_H in all the nanoemulsions (without RNA) had comparable values of 180 ± 2 nm pre-aerosolization, 183 ± 2 nm after Aeroneb, and 175 ± 2 nm after Syringe neb, averaged over three independent measurements of different batches of the nanoemulsion (Figure 2b). Figure 2c shows that the PDI of the nanoemulsions nearly doubled after aerosolization and reached a value of 0.22. This observed increase in PDI is consistent with previous studies of aerosolized drug delivery systems , suggesting that some increase in size distribution heterogeneity is typical during the aerosolization process while still maintaining pharmaceutical acceptability [50]. The zeta potential of the nanoemulsions decreased from 20 mV pre-neb to 12 mV and 17 mV for Aeroneb and Syringe neb, respectively (Figure 2d). Aerosolization can decrease zeta potential because the process typically concentrates solutes and ions in the droplet which compresses the electric double layer, resulting in a decreased zeta potential [51-53].

The nanoemulsions exhibited a spherical core-shell architecture as visualized by TEM, where the PFOB core was stabilized by a PAMD-C/miRNA shell layer (Figure 2e). This structural organization allowed for the presentation of PAMD-C and its CXCR4-binding moieties on the emulsion surface, thereby maintaining the positive surface charge required for miRNA binding. Cryo-TEM revealed distinct morphological changes in the nanoparticle structure following nebulization (Figure 2e). Both pre- and post-nebulized samples exhibited discrete, well-defined nanoparticles with clear core-shell boundaries.

2.2 Formulation and stability of RNA nanocapsules

The RNA nanocapsule was formulated by mixing PAMD-C@PFOB nanoemulsion and miRNA at different nanoemulsion-to-miRNA weight ratios (w/w) ranging from 0.5:1 to 10:1 in 10 mM HEPES buffer (pH 7.4) and incubating at room temperature for 30 min. The nanoemulsion condensing ability for miRNA was assessed using gel electrophoresis (Figure 2f). Colloidally stable nanocapsules with completely bound miRNA were formed at PAMD-C polymer to

miRNA w/w ≥ 2. The D_H of the nanocapsules at w/w values of 2, 4, and 8 were all reduced relative to the neat nanoemulsion without the miRNA, with values as low as 158 nm for w/w 2 and 163 for w/w 4, which is ~10-13% less than the D_H of the neat nanoemulsion (Figure 2g). Reduction in nanoparticle size with increasing surface density of RNA likely stems from stronger electrostatic interactions with positive charged polymers, which has also been observed in other condensates [54]. Additionally, while the zeta potential of the nanocapsules formulated at w/w of 2 and 4 (18 mV) was reduced slightly with respect to the neat nanoemulsion (21 mV), the residual positive zeta potential indicated that PAMD-C cationic moieties are present on the nanocapsule surface and not fully engaged in electrostatic interation with miRNA (Figure 2h). Hence, subsequent in vitro and in vivo studies were conducted using a w/w ratio of 4, so that the slight excess of CXCR4-binding moieties could enable targeting of CXCR4-overexpressing cells.

To evaluate the CXCR4 binding capabilities of our nanocapsules, we performed a CXCR4 redistribution assay, a standard method for evaluating CXCR4 antagonists. The nanocapsules demonstrated a concentration-dependent inhibition of CXCR4 receptor internalization, following SDF-1 stimulation (Figure S3), confirming the ability of the nanocapsules to effectively bind to CXCR4 receptors.

Further, studies carried out to check stability of the system demonstrated that the size of the RNA nanocapsules increases minimally by 20% over three days at room temperature, which is negligible compared to the rapid 113% increase in D_H values for the PAMD-C@PFOB nanoemulsion (Figure 2i). Finally, luciferase gene knockdown study was done in 4T1 cells stably expressing luciferase (4T1.Luc), to study preservation of the RNA functionality post nebulization. While Luc gene silencing observed in Syringe neb and pre-neb samples were comparable, Aeroneb showed a ~ 41% increase in Luc gene silencing activity (Figure 2j). This improved transfection efficiency observed with Aeroneb aerosolized nanocapsules likely stems from their reduced zeta potential (Figure 2d), which represents an optimal balance of positive charge. While positive charge is necessary for interaction with negatively charged cell membranes, excessively high positive charge can cause cytotoxicity. The moderately positive zeta potential of Aeroneb-delivered nanocapsules appears to strike an ideal balance that maintains sufficient electrostatic attraction for cellular uptake, thereby enhancing transfection efficiency [55].

2.3 Characterization of RNA nanocapsule aerosols

In order to effectively deliver the nanocapsules to lung tumors, it is essential that the aerodynamic diameter of the aerosolized nanocapsules is appropriate for targeting the specific lung region where the tumor is located. For tumors in the peripheral lung regions where many lung adenocarcinomas develop, particles of 1-5 μm diameter are required to achieve optimal deposition. The schematic of the NGI setup is presented in **Figure 3a**. The NGI is a seven stage cascade impactor consisting of 8 collection cups with the following size range cut-offs: 14.10 μm, 8.61 μm, 5.39 μm, 3.30 μm, 2.08 μm, 1.36 μm, 0.98 μm, and a final micro-orifice collector (MOC) of 0.3 μm (Figure 3b). The droplet size distribution obtained from APS is shown in Figure 3c. The droplets of RNA nanocapsule solution aerosolized using Aeroneb appear to be dominated by a single log-normal mode. The total distribution has a peak aerodynamic diameter (Dp) value of ~1 μm and a tail that extends out to 3 μm. The RNA nanocapsules aerosolized using the syringe neb appear to be composed of multiple log-normal modes. The total distribution has a peak Dp value of ~2.1 μm and a tail that extends out to 12 μm. The fluorescence intensity measured from Cy3 labelled nanocapsules was used to calculate the deposition amount at each stage of the NGI. The stage deposition (%) in Figure 3d is defined as the concentration recovered at each stage normalized by the total recovered concentration. Both the Aeroneb and Syringe neb samples have a clear deposition spike at stage S7 (0.98 μm), and reduced depositions at stages S4, S5, and S6. Overall, the aerodynamic size of the RNA nanocapsule using both nebulizers is conducive to deep lung deposition. Results from in vivo expeirments in further sections confirm these hypotheses.

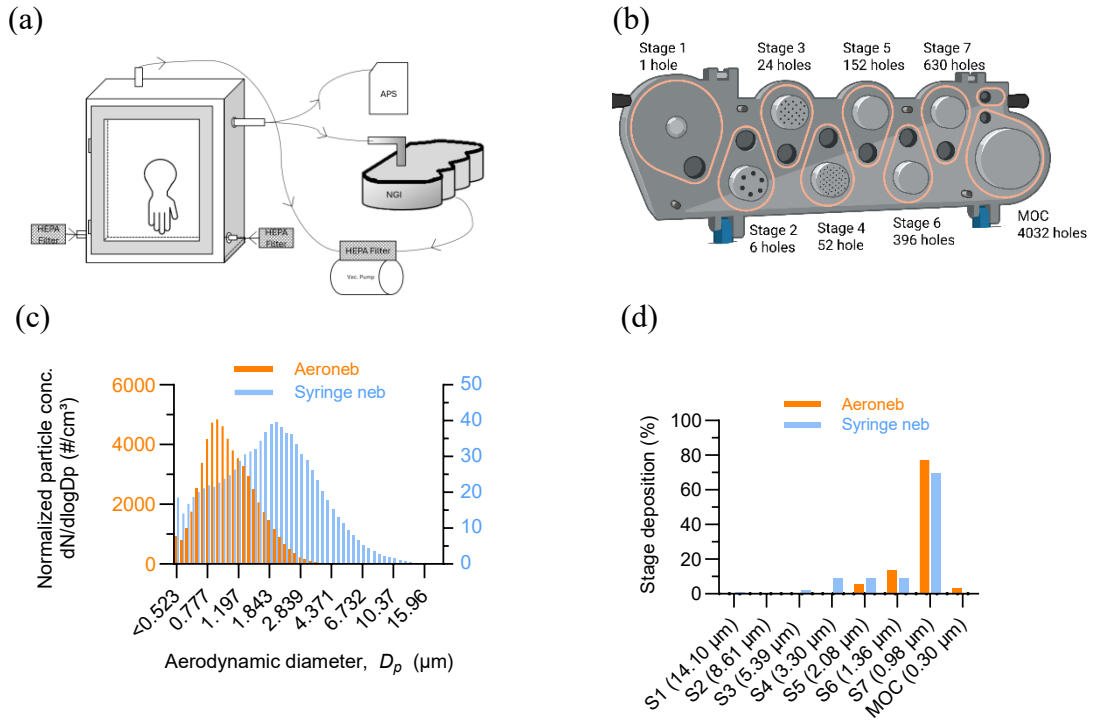

Figure 3. Characterization of PAMD-C@PFOB/miRNA nanocapsule aerosols. (a) Schematic of upwelling flow chamber with NGI and APS units. (b) Schematic of the Next Generation Impactor (NGI) from MSP, a high-performance cascade impactor with seven stages and a Micro-Orifice Collector (MOC) at the end (*Figure created with Biorender.com)* (c) Aerodynamic particle size distribution from APS and (d) Fluorescence intensity from Cy3-labelled aerosolized RNA nanocapsules across different stage cut-off diameters of the NGI at 15 L/min.

2.4 In vitro cytotoxicity and cellular uptake of RNA nanocapsules

The cytotoxicity of nanoemulsions and RNA nanocapsules was evaluated in 4T1-Luc and H1975-Luc human non-small cell lung carcinoma cell lines using CTB viability assay. The nanoemulsions demonstrated differential toxicity profiles, with IC50 values of 12.12 µg/mL and 7.24 µg/mL of PAMD-C polymer in 4T1.Luc and H1975.Luc cells, respectively (Figure S4a). RNA nanocapsules loaded with scrambled miRNA exhibited minimal cytotoxicity, maintaining cell viability above 90% at miRNA concentrations up to 150 nM (0.2 µg) and PAMD-C concentration of 0.80 µg (w/w 4) (Figure S4b).

Next, cellular uptake of RNA nanocapsules containing Cy3-labelled PAMD-C and FITC-labelled miRNA was assessed in 4T1 cells. We observed cytoplasmic colocalization of PAMD-C@PFOB-Cy3 (red) and miRNA-FITC (green) (**Figure 4a**), important step to enable access to the RNA interference machinery.

Flow cytometric analysis revealed that the transfection potency of the RNA nanocapsules was dependent on the w/w ratio of the polymer and the RNA. RNA nanocapsules formulated at w/w 4 were taken up by 58% of the cells, while increasing the w/w ratio to 6 resulted in uptake by only 40% of the cells (Figure 4b). Nanocapsules with lower w/w ratios have lower zeta potentials (Figure 2h) and more efficient transfection, which is also similar to the trends reported earlier in Figure 2d and Figure 2j.

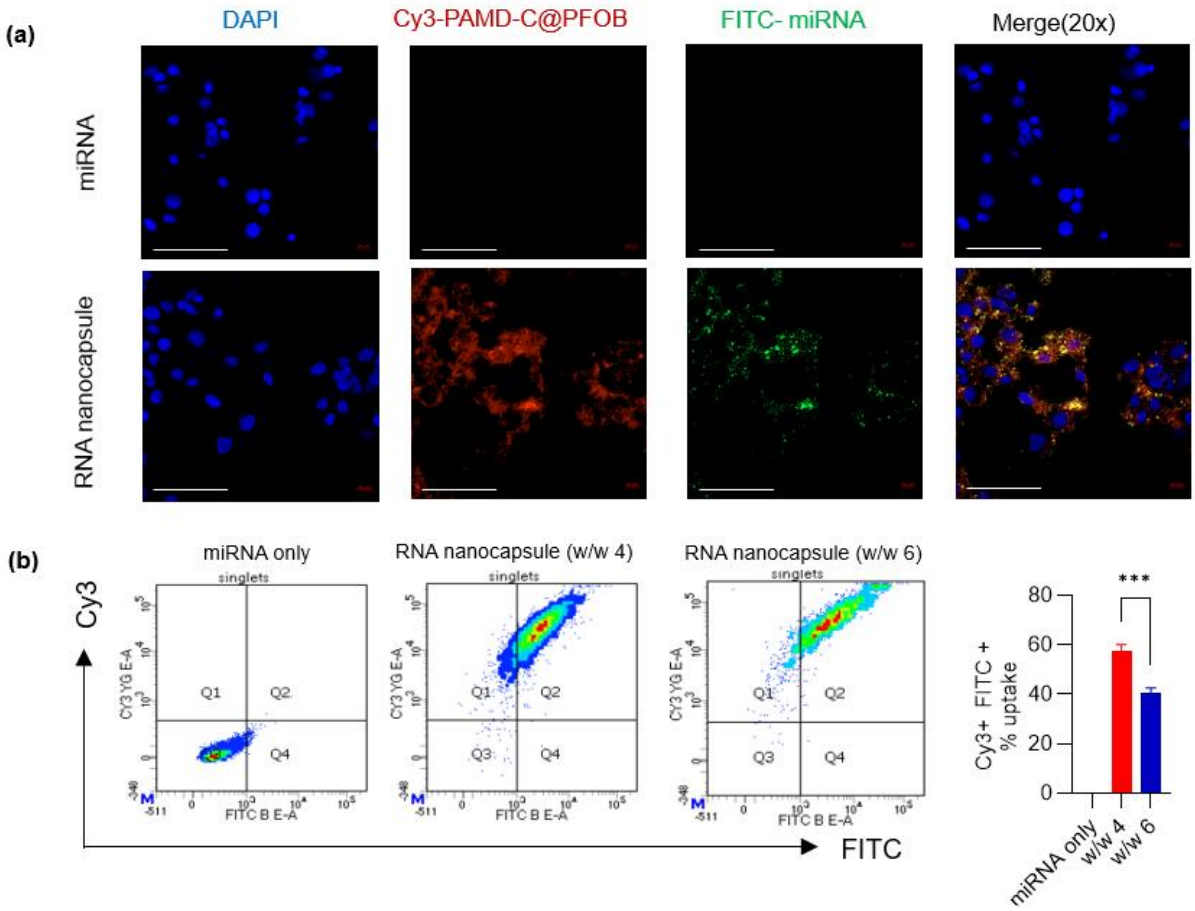

Figure 4. Cellular uptake of PAMD-C@PFOB/miRNA nanocapsules. a) Confocal microscopy images demonstrating cellular uptake of RNA nanocapsules (150 nM miRNA) after 6 h incubation in 4T1 cells. Scale bar = 20 µm. b) Cellular uptake of RNA nanocapsules at different w/w ratios by flow cytometry. n = 3 per group , *** $p < 0.001$.

2.5 Pulmonary delivery of aerosolized RNA nanocapsule

RNA therapeutics often show limited anti-cancer efficacy due to poor tumor penetration, retention and insufficient interaction with the tumor microenvironment. To evaluate the extent of retention of the nanocapsules in the lungs as well as the tumors, we conducted biodistribution studies in both healthy and Lung Metastatic Breast Cancer (LMBC) mice. We administered

dual-labeled RNA nanocapsules (Cy3-PAMD-C@PFOB/Cy5.5 miRNA) at a dose of 20 µg miRNA and 80 µg PAMD-C in 60 µL. The dose was selected based on previous reports from our lab [56]. The dual fluorescent labeling enabled tracking of both the delivery vehicle and the therapeutic cargo. Enhanced accumulation of Cy5.5-labeled miRNA in the lungs was observed compared to other major organs, for both healthy and LMBC mice (left and right panels in **Figure 5a**). Figure 5b depicts the Cy5.5 fluorescence signal from the miRNA retained in the lungs of healthy and LMBC mice at different time points post administration. At 24 h, the average radiance in the LMBC mice lungs is 1.5 times higher than the average radiance in the healthy mice lungs, signaling longer retention of the nanocapsules by the tumor mice. Moreover, in healthy mice, the significantly decreased intensity of the Cy5.5 signal in the lungs at 48 h indicates that the miRNA is getting cleared from the lungs after 24 h (Figure 5b). On the other hand, there is no significant decrease in the Cy5.5 signal intensity in the LMBC mice lungs between 24 and 48 h (Figure 5b). This enhanced retention in tumor-bearing lungs likely results from multiple factors: the enhanced permeability and retention (EPR) effect allowing passive accumulation in tumor tissue and sequestration by the mononuclear phagocyte system (MPS) of the lung, which has been shown to retain perfluorocarbon-based nanoparticles [57].

Administering the miRNA to the lungs should result in the highest levels of fluorescence immediately following administration, followed by gradual reduction due to clearance from the lungs. However, the data in Figure 5b shows comparable or even higher fluorescence intensities at 24 h and 48 h, compared to the values at 6 h and 12 h. This trend points towards a controlled release of the miRNA payload from the nanocapsule due to their disassembly in the cells. To test this hypothesis, we examined the nanocapsules under three conditions: i) Cy5.5 miRNA, ii) nanocapsule with Cy5.5 miRNA, and iii) nanocapsule with Cy5.5 miRNA and Heparin. As seen in Figure 5c, the fluorescence signal is significantly quenched when the miRNA is in the nanocapsule, relative to bare miRNA (blue vs red bars), likely due to the close proximity of the Cy 3 and Cy 5.5 fluorophores. Upon adding heparin to the nanocapsules, the fluorescence signal increases to levels comparable to that of the bare miRNA, demonstrating heparin-mediated release of miRNA from the nanocapsule. This observation demonstrates that the miRNA is not instantaneously released from the carrier nanocapsule after administration, as evident from the relatively weak average radiance at 6 h and 12 h. At longer times (24 h and 48 h), the miRNA is released from the nanocapsule once taken up by the lung cells, especially in tumor mice. Detailed results from flow cytometry experiments in the following sections show miRNA uptake in various lung cell populations.

To assess lung penetration, we analyzed the intra-pulmonary distribution of the labeled RNA nanocapsules 24 h post aerosolized administration, using confocal microscopy. We observed co-localization of both fluorescent markers in epithelial cells surrounding the alveoli in healthy mice (Figure 5d). This colocalization suggests that the miRNA maintained their structural integrity throughout the delivery process while undergoing gradual release at the target site. Furthermore, we observed that the RNA nanocapsules successfully penetrated all pulmonary lobes within 6 h of administration. To specifically evaluate delivery of the RNA nanocapsules to the tumors in the lung, we utilized 4T1 cells stably expressing mCherry to generate the lung metastatic tumors. Confocal microscopy revealed clear colocalization between the Cy5.5-labeled miRNA, Cy3-labelled nanoemulsions and mCherry-expressing tumor cells, confirming successful delivery of the RNA nanocapsules into the metastatic lesions (Figure 5e).

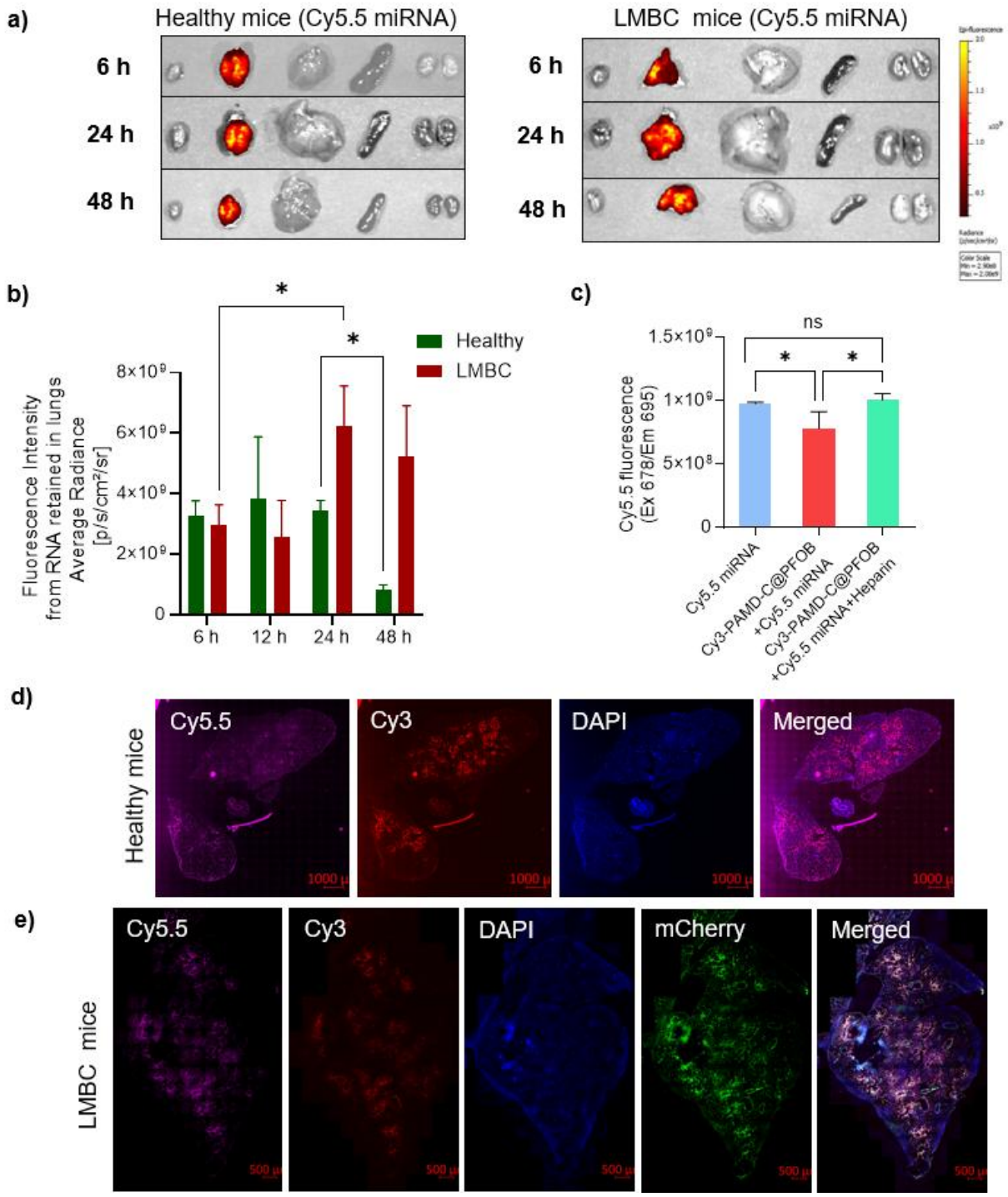

Figure 5. Biodistribution of PAMD-Ch@PFOB/miRNA nanocapsules in healthy and LMBC mice. (a) Representative ex-vivo fluorescence images of major organs at different time points post aerosolized administration of nanocapsules in healthy and LMBC mice. b) Mean fluorescence intensity of the miRNA retained in the lungs of healthy and LMBC mice at different time points post-aerosolized administration of the nanocapsules (c) Fluorescence intensity from Cy5.5 miRNA with and without complexation to Cy3-PAMD-C@PFOB nanoemulsion. (d) Representative confocal images of lung sections 24 h post administration of labeled RNA nanocapsules in healthy mice. Scale bar = 1000 µm . (e) Representative confocal

images of lung sections 24 h post administration of labeled RNA nanocapsules in LMBC mice injected with 4T1-Luc-mCherry cells. Scale bar = 500 µm. n = 3 per group . * $p < 0.05$, ns- not significant.

2.6 Inflammatory response and cellular distribution of the RNA nanocapsules in lung tissue of healthy and LMBC mice

To evaluate potential inflammatory response induced by the RNA nanocapsule in healthy mice, a 40 cytokine array was performed 12 h post-administration (Figure S5). **Figure 6a** shows that only two cytokines, CXCL1 and TIMP-1, were highly upregulated compared to placebo when threshold for fold change was set at 1.5. The upregulation of TIMP-1 may be linked to the interaction between TIMP-1 and the CXCR4 signaling axis. TIMP-1 has been shown to influence CXCR4-mediated pathways, which play a role in immune cell recruitment, activation and tissue remodeling [58]. Disrupting this axis by the CXCR4 antagonizing nanocapsules can enhance their expression and affect immune cell homeostasis in the lungs. Additionally, CXCL1 has been implicated in promoting neutrophil migration and activation, processes that are often transient during inflammatory responses. CXCR4 antagonists, such as AMD3100, have been shown to modulate chemokine levels, including CXCL1, in a time-dependent manner [59]. This suggests that the upregulation of TIMP-1 and CXCL1 likely represents a transient immune activation phase triggered by the CXCR4 antagonistic properties of our delivery system, potentially serving as a protective mechanism to regulate inflammation and promote tissue repair in healthy mice.

The rapid clearance of therapeutic formulations by immune cells poses a significant challenge for effective pulmonary delivery. Phagocytic cells such as macrophages and other lung resident immune cells rapidly recognize and engulf foreign materials, reducing the bioavailability and efficacy of treatments intended for non-immune target cells. To evaluate our delivery system's ability to evade this clearance mechanism, we first conducted flow cytometric analysis to evaluate uptake of Cy5.5-labeled miRNA by different CD45+ pulmonary immune cells in healthy mouse lungs. Results revealed that only 2-6 % of the administered dose was taken up by various pulmonary immune cells indicating effective evasion of immune recognition (Figure 6 b). This limited uptake by pulmonary immune cells is advantageous for applications targeting non-immune cells that necessitate prolonged localization in the intended target cells to achieve optimal therapeutic efficacy.

The distribution of miRNA across lung epithelial and endothelial cells (CD45-) was also analyzed. We found that ~80% of type II alveolar cells and 70% of bronchial epithelial cells have taken up the nanocapsules, while other analyzed cell types demonstrated less than 5% uptake (Figure 6c). Analysis of the total miRNA dose distribution revealed that type II alveolar cells accounted for approximately 60% of the administered dose, while bronchial epithelial cells which line the conducting airways of the lungs from trachea to the terminal bronchioles contributing 30% (Figure 6d). The remaining cell types, including type I alveolar, vascular and lymphatic endothelial cells, collectively accounted for less than 10% of total uptake. This preferential accumulation in type II alveolar and bronchial epithelial cells can be attributed to their robust endocytic activity [60-61]. Conversely, the limited uptake observed in other cell types likely stems from differences in their glycocalyx composition, affecting nanoparticle binding and internalization [62-64]. Similarly, in LMBC mice, most of the miRNA was taken up by type II alveolar cells (Figure 6e and f), with relatively low uptake by other cell-types. Lastly, Figure 6g shows that the polymer and miRNA uptake by 4T1.mcherry cells of LMBC mice was 60% and 38%, respectively, demonstrating RNA nanocapsule delivery to the tumor cells.

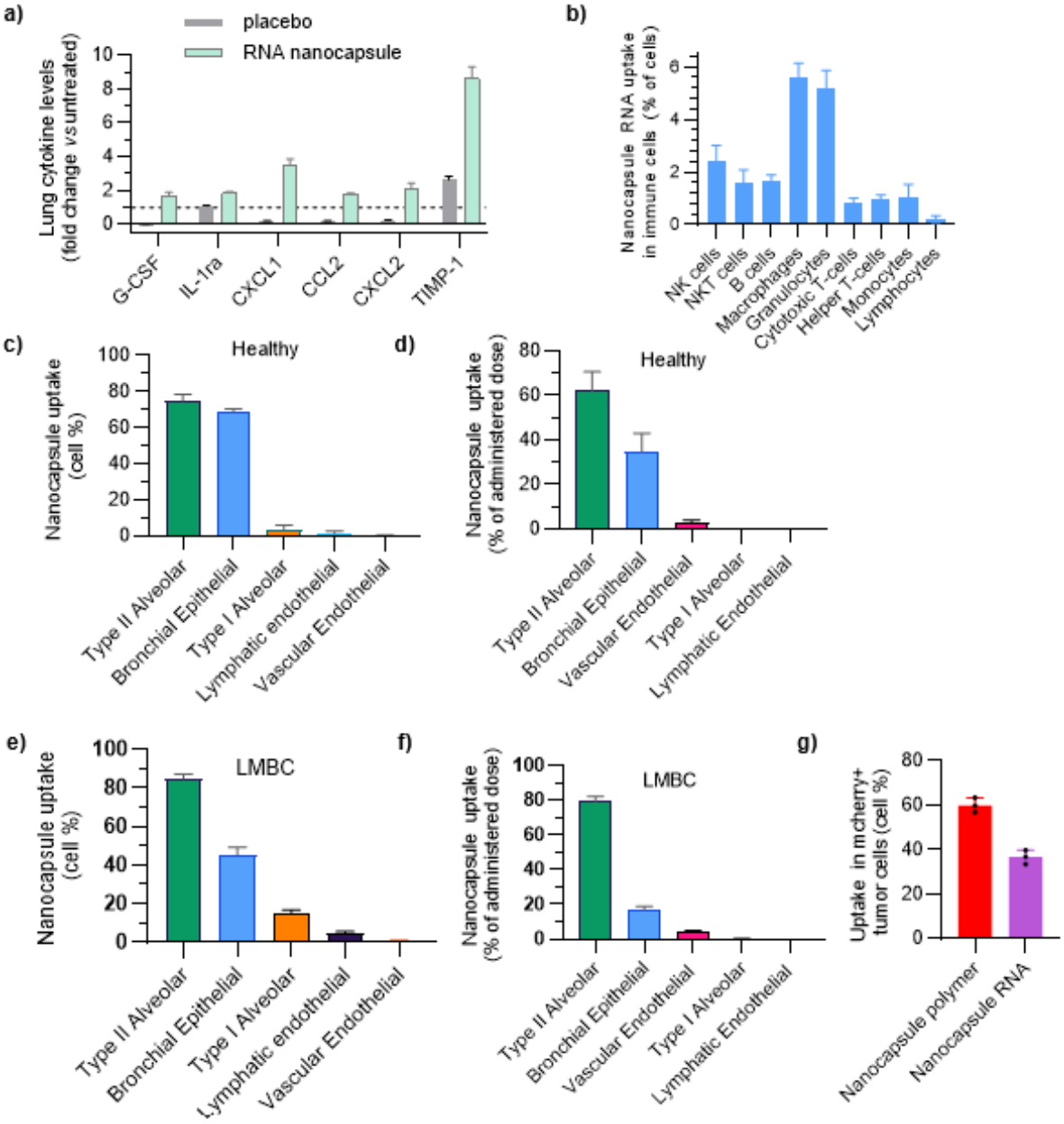

Figure 6. Cellular distribution and safety assessment of miRNA nanocapsules in healthy and LMBC-mCherry mouse lungs. a) Pulmonary immune response profile following RNA nanocapsule administration. Analysis of lung tissue protein lysates from healthy controls, placebo-treated (DI H_2O 60 µl), and RNA nanocapsule-treated (20 µg miRNA) mice at 12h post-administration (n = 3). A panel of 40 immune mediators was evaluated, including cytokines (TNF, IL-6, IL-12p70, IL-1β, IFNγ, IL-2, IL-17, IL-5, IL-16, TIMP1, TREM1, IL-23, IL-10, IL-1ra, IL-13 and IL-4), chemokines (CCL1, CCL2, CCL3, CCL4, CCL5, CCL11, CCL12, CCL17, CXCL1, CXCL2, CXCL9, CXCL10, CXCL11, CXCL12 and CXCL13), growth factors (G-CSF, GM-CSF, M-CSF, IL-3 and IL-7) and cell adhesion molecules (CD54 and complement component 5a) (Data are presented as mean fold change relative to healthy controls. Raw images are shown in Fig. S5. (b) Flow cytometric analysis of immune cell populations showing uptake of Cy5.5-labeled nanocapsule miRNA in healthy mouse lungs 4 h post-administration. Distribution of Cy5.5 labeled nanocapsule miRNA in healthy mouse lung CD45- populations, showing (c) percentage uptake per cell type and (d) percentage of total administered dose. (e,f) Similar analysis in LMBC mouse lungs showing (e) cellular uptake and

(f) total dose distribution in CD45- subtypes. (g) Uptake of Cy3- labeled nanocapsule polymer and Cy5.5- labeled nanocapsule miRNA by 4T1-mCherry tumor cells isolated from the lungs of LMBC mice.

2.7 Aerosolized miR-34a delivery via RNA nanocapsules suppresses tumor growth in LMBC model

In light of the resistance of metastatic breast cancers to immune checkpoint blockade therapy, we investigated the therapeutic potential of miR-34a nanocapsules using a lung metastasis model. miR-34a, which is downregulated in various cancers including lung and breast cancer, acts as a tumor suppressor and regulates expression of immune checkpoint proteins like PD-L1 [65]. We hypothesized miR-34a could effectively treat lung metastases through its pleiotropic effects on multiple cellular pathways, including PDL1-mediated immune regulation, cell survival, metastasis, and tumor progression networks [65-67]. Following tumor implantation, the animals were treated with aerosolized RNA nanocapsules on days 6, 10, and 14 (**Figure 7a**). Controlled animals received placebo and nab-paclitaxel chemotherapy (10 mg/kg) via intravenous administration on days 5 and 9.

In vivo bioluminescence imaging on day 16 revealed differential treatment responses across groups. While the nab-paclitaxel group showed moderate tumor inhibition, the miR-34a group demonstrated significant tumor inhibition (Figure 7b). The total bioluminsecent flux from the luciferase-expressing tumor cells in the miR-34a treated mice was reduced by nearly tenfold compared to the untreated mice. H&E staining of lungs harvested on day 16 further supported the observation as shown by the miR-34a group exhibiting a drastically reduced metastatic burden, with smaller and fewer lung metastases compared to the nab-paclitaxel group (Figure 7c). In addition to the therapeutic outcomes resulting from miR34a treatment, we hypothesize that the CXCR4 antagonism by the nanocapsules may have contributed to reduced tumor burden [68-69]. Survival analysis further demonstrated the superior therapeutic efficacy of miR-34a nanocapsules. While nab-paclitaxel treatment modestly extended median survival from 24 to 35 days, miR-34a nanocapsule therapy significantly doubled the survival of the placebo group to 47 days, despite cessation of treatment after day 14 (Figure 7d). This substantial survival benefit, achieved with just three doses of the nanocapsule, suggests that additional treatment cycles beyond day 14 could potentially yield further improvements in survival outcomes.

Body weight trends also showed major differences between the various treatment groups. Placebo group experienced a steep decline in body weight by ~25% within three weeks. Similarly, the body weight of the nab-paclitaxel treated mice was reduced by 15% within ten days – likely due to the effects of chemotherapy given on days 5 and 9, and later after three

weeks, due to recurrent tumors at later stages. In contrast, the mice receiving miR-34a nanocapsules showed steady or gradually increasing body weights over four weeks (Figure 7e). This initial progress was observed after just three doses, with body weight monitored for only 30 days. As no additional doses were administered, any residual tumor cells in the miR34a group could have potentially proliferated, leading to death at around day 50.

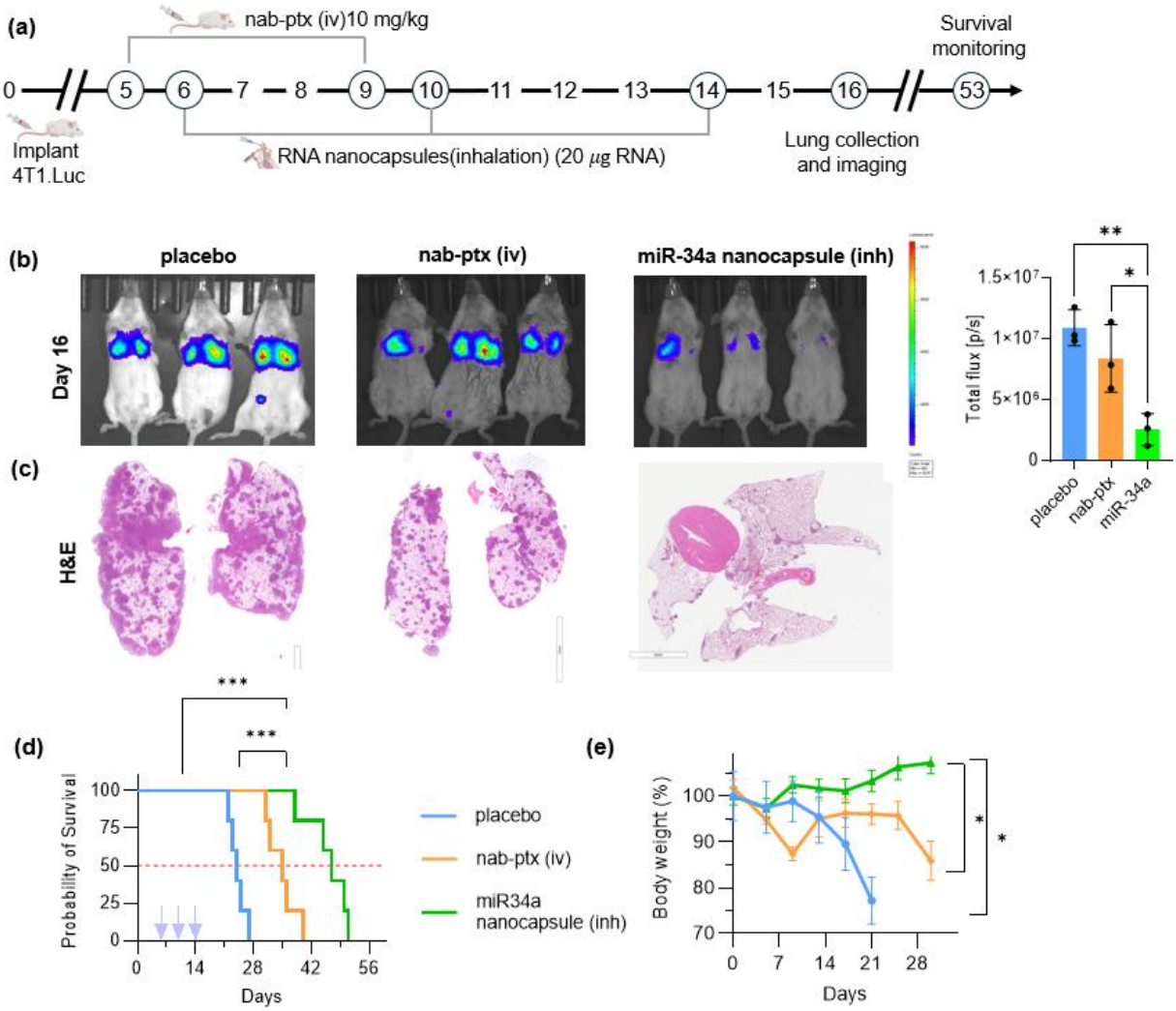

Figure 7. In vivo antitumor efficacy of the miR-34a nanocapsules in LMBC mice. (a) Experimental timeline showing the dosing regimen for LMBC mice (b) In vivo bioluminescence imaging and quantification of total bioluminescent flux from the lungs of LMBC mice post different treatments. (c) H&E staining of lung tissues collected on day 16 (scale bar, 5mm). (d) Survival curves after different treatments (n=5) analyzed using log-rank test. Median survival: placebo (24 days), nab-ptx (35 days), miR34a nanocapsule (47 days) (e) Plots representing percentage body weight change in the different treatment groups (n = 5). *** $p < 0.001$, ** $p < 0.01$, * $p < 0.05$

Immunohistochemical (IHC) analysis was performed to evaluate the treatment effects on tumor proliferation, metastatic burden, apoptosis, and leukocyte infiltration in the lung. Ki67, a marker for cell proliferation, was significantly reduced in both the nab-ptx and miR-34a nanocapsule

groups compared to the placebo (**Figure 8a**). Notably, only 2% of the total cells were Ki67+ in the nanocapsule group, which is a two-fold decrease compared to the nab-ptx group and a four-fold decrease compared to the placebo group. This trend was mirrored in Epcam staining, a marker for epithelial-derived carcinomas, where miR-34a treatment induced a substantially larger reduction in Epcam+ cells compared to nab-ptx (78% vs 40%), indicating reduced epithelial characteristics and tumor regression (Figure 8b). Conversely, the percentage of Cleaved Caspase 3 positive (CC3+) cells indicative of apoptosis, was significantly increased in both treatment groups, with miR-34a again demonstrating a stronger pro-apoptotic effect compared to nab-ptx (Figure 8c).

The miR-34a group exhibited a significant decrease in the net abundance of CD45+ cells as demonstrated in Figure 8d as shown by ~50 % decrease of CD45+ cells compared to both the nab-ptx and placebo groups. This significant reduction is reflective of the marked decrease in Granulocytic Myeloid-Derived Suppressor Cells (G-MDSCs) within the lungs (**Figure 9c**). Since G-MDSCs represent a major component of the CD45+ infiltrate in the 4T1 model and are known to increase proportionally with tumor burden, this significant reduction in CD45+ cells in the miR34a group suggests an alleviation of the tumor burden [70].

Lastly, Figure 8e demonstrates a reduction in F4/80+ levels (a marker for tissue-resident immune cells, typically of monocytic lineage such as macrophages and monocytes) by approximately 10% in the nab-ptx treated group and approximately 50% in the miR34a treated group, compared to the placebo group. This reduction is likely significant because F4/80 contributes to peripheral tolerance by promoting the induction of inducible regulatory T cells (iTregs) [71]. These iTregs can produce anti-inflammatory cytokines, which can foster oncogenesis and proliferation. Therefore, the substantial decrease in F4/80+ cells observed in the miR-34a group likely indicates a shift towards a more immune-permissive environment, conducive to immune-mediated tumor clearance.

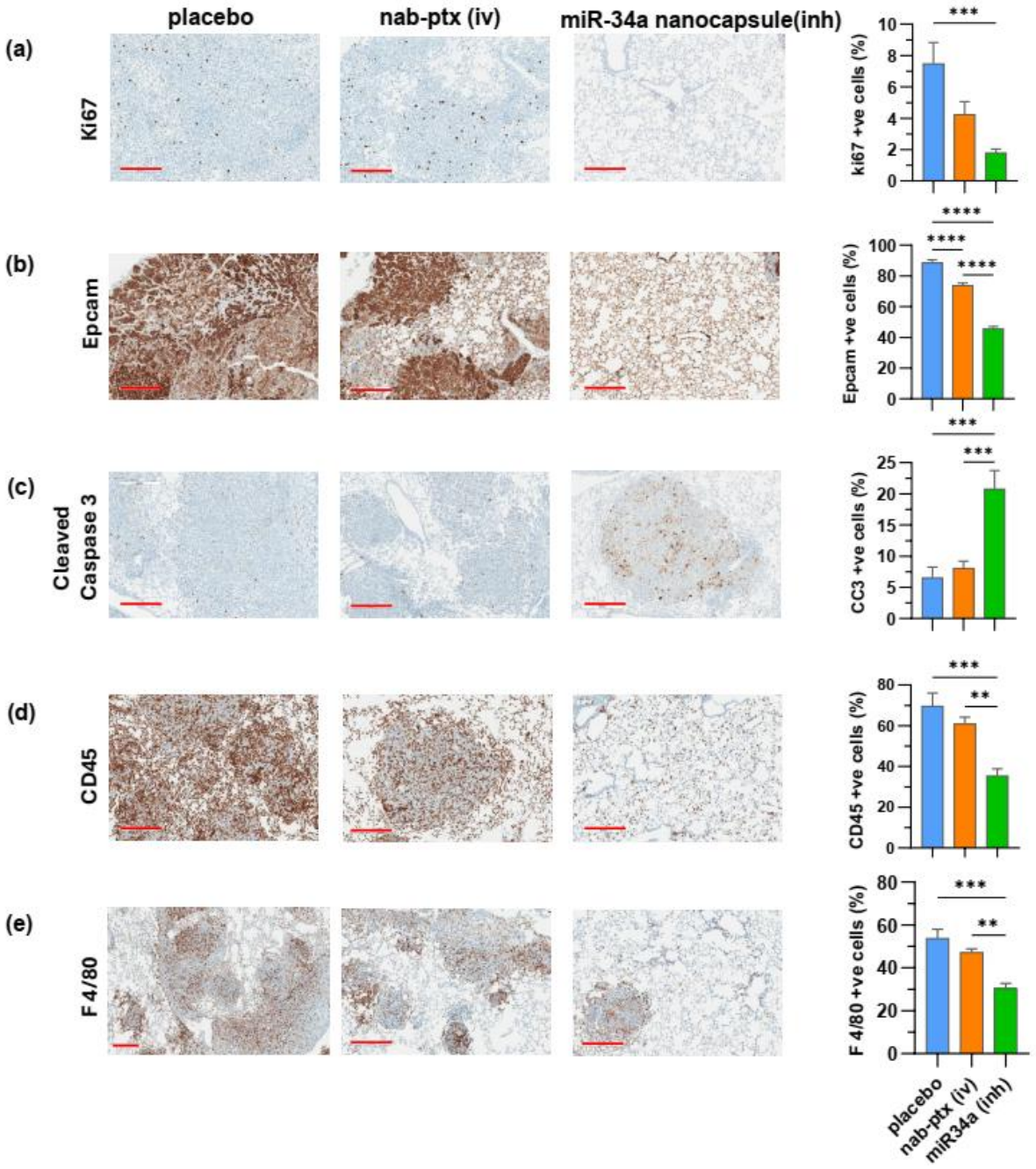

Figure 8. Analyses of treatment effect of miR34a nanocapsules on selected biomarkers in lung metastases. Representative images of immunohistochemical staining across different treatment groups and Percentage of positively stained area for a) Ki67 b) Epcam (c) Cleaved Caspase 3 (CC3) (d) CD45 (e) F4/80. n = 3 mice per group. Areas in the sections having metastatic tumors only were quantified. ImageJ was used for quantification of the images. Three fields for each section was quantified. Scale bar = 300 µm. **** $p < 0.0001$, *** $p < 0.001$, ** $p < 0.01$.

2.8 Aerosolized miR34a nanocapsule treatment induced immune cell infiltration in the metastatic tumors and enhanced immunotherapy response

To investigate the impact of miR-34a nanocapsule therapy on immune modulation within the TME and its potential to enhance anti-tumor immunity, we analyzed the composition of CD45+

cells in metastatic lungs. Given the importance of T cell infiltration for enhanced immunotherapy response, we hypothesized that the combined effects of miR-34a overexpression and CXCR4 blockade by PAMD-C would synergistically promote T cell infiltration and decrease the levels of immunosuppressive cells, thereby enhancing anti-tumor immunity.

Our results demonstrate a significant increase in CD8+ T cell infiltration in miR-34a group (**Figure 9a**). While placebo and nab-ptx groups exhibited only ~1% cytotoxic T cells in the total live cell population, the miR-34a group showed nearly 8%. CD8+ T cells play a crucial role in cancer by identifying and eliminating aberrant cells including metastatic cells [72]. However, the TME presents a hostile environment characterized by high antigen exposure, and nutrient deprivation, often driving CD8+ T cells towards terminal exhaustion, a state characterized by loss of effector function and eventual cell death [73-74]. The observed increase in infiltrating CD8+ T cells in the miR34a treated group is indicative of the environment becoming more permissive to immune-mediated tumor clearance. This finding aligns with the expected effects of CXCR4 axis antagonism, which is known to enhance CD8+ T cell infiltration into tumors by disrupting the CXCL12/CXCR4 chemokine gradient that normally restricts T cell trafficking, reducing immunosuppressive stromal components, and downregulating PD-L1 expression on tumor cells thus alleviating immunosuppression [75]. The increase in CD8+ T cells in the miR34a treated group was further supported by a substantial rise in CD4+ helper T cells. Compared to the placebo and nab-ptx groups, which exhibited only ~5% CD4+ T cells, the miR-34a treated group showed a significant increase to ~22% (Figure 9b). This substantial expansion of CD4+ T cells in the miR34a group suggests a reinvigorated immune response within the TME, given their crucial role in supporting and enhancing CD8+ cytotoxic T cell recruitment, proliferation and effector function within the TME [76].

Further, miR34a nanocapsule group demonstrated a significant reduction in granulocytic myeloid-derived suppressor cells (G-MDSCs), with levels decreasing from about 60% in the placebo and 45% in the nab-ptx group to 30% in the miR-34a group (Figure 9c). As G-MDSCs utilize immunosuppressive mechanisms to inhibit anti-tumor immune responses [77], their significant reduction suggests a broad attenuation of immunosuppressive signals within the TME [78]. This likely contributes to the observed increase in T cell infiltration and activation, ultimately enhancing the potential for T-cell effector function [79-80].

The decrease in macrophages, from ~ 7% in the placebo to ~ 1% in the miR-34a group (Figure 9d), can be attributed to disruption of the CXCR4-SDF1 axis. CD11b+ cell chemotaxis, which inherently includes macrophages, is prone to influence via modulation of the CXCR4-SDF1 axis. Due to antagonism of CXCR4 by PAMD-C, CD11b+ cell infiltration is likely hindered; this phenomenon has been demonstrated by studies showing that CXCR4 blockade inhibits CD11b+ cell chemotaxis in response to CXCL12 in bone fracture and bleomycin-induced lung injury models [81]. This reduction in CD11b+ macrophages could be beneficial, as these highly plastic cells are prone to adopting an anti-inflammatory polarization state within the TME, further exacerbating the existing immunosuppressive environment [82].

A significant reduction (>50%) was observed in natural killer (NK) cells in the miR34a treated group compared to the placebo group (Figure 9e). This finding is likely attributable to miR-34a mediated downregulation of ULBP2, an NK cell immune-receptor ligand, essential for NK cell mediated tumor recognition and lysis [83]. While miR-34a demonstrates robust anti-cancer effects through other mechanisms, its downregulation of ULBP2 potentially compromises NK cell activity. Therefore, despite the substantial immunomodulatory effects achieved in the TME by our inhalable miR-34a nanocapsule, the observed NK cell reduction stems from miR-34a's inherent properties, independent of the delivery system's efficacy.

Critically, these observed immune changes correlate with a decrease in PD-L1 mRNA levels in the miR-34a group (Figure 9f). It has been reported that 4T1 tumors naturally produce granulocyte-colony stimulating factor (G-CSF), a pro-granulopoietic growth factor that also drives G-MDSC proliferation and mobilizes neutrophils which ultimately differentiate into G-MDSCs within the tumor [84]. Because of the inherent contributions of G-MDSCs to the anti-inflammatory milieu of the tumor, they foster the upregulation of PD-L1, thereby bolstering the anti-inflammatory environment. PD-L1, a key regulator of immune suppression, is frequently upregulated in tumors and contributes to leukocyte exhaustion and death [85]. The significant reduction in PD-L1 suggests both a decrease in tumor burden and an alleviation of the immunosuppressive TME, fostering a more favorable environment for infiltrating and resident leukocytes. The reduction in PD-L1 mirrors the observed increases in T cell infiltration and abundance (Figure 9a, b), as it removes a major inhibitory signal that would otherwise limit their anti-tumor activity.

Also, miR-34a nanocapsule treatment led to decreased CXCR4 mRNA levels (Figure 9g). This reduction in CXCR4 signaling has important implications for the TME through multiple

mechanisms. First, decreased CXCR4 activity likely reduces the population of terminally exhausted T cells (T_{ex}) while promoting functional CD8+ T cell infiltration, potentially through modulation of the JAK2-STAT3 pathway [86]. Additionally, since CXCR4 is a key driver of cancer progression, metastasis, and angiogenesis [87], its downregulation by miR-34a nanocapsules may directly inhibit these tumor-promoting processes. Interestingly, while CXCR4 downregulation represents a desirable outcome, it potentially creates a feedback mechanism wherein subsequent doses of the nanocapsules may experience diminished targeting efficiency due to reduced receptor availability. This dynamic relationship between therapeutic effect and targeting efficiency highlights the importance of carefully optimized dosing schedules and suggests potential benefits of combination targeting strategies for sustained therapeutic efficacy. Together, these findings suggest that the therapeutic efficacy of inhalable miR-34a nanocapsules against lung metastases stems from their dual action: enhancing anti-tumor immunity while simultaneously disrupting CXCR4-dependent processes that support tumor growth and metastases.

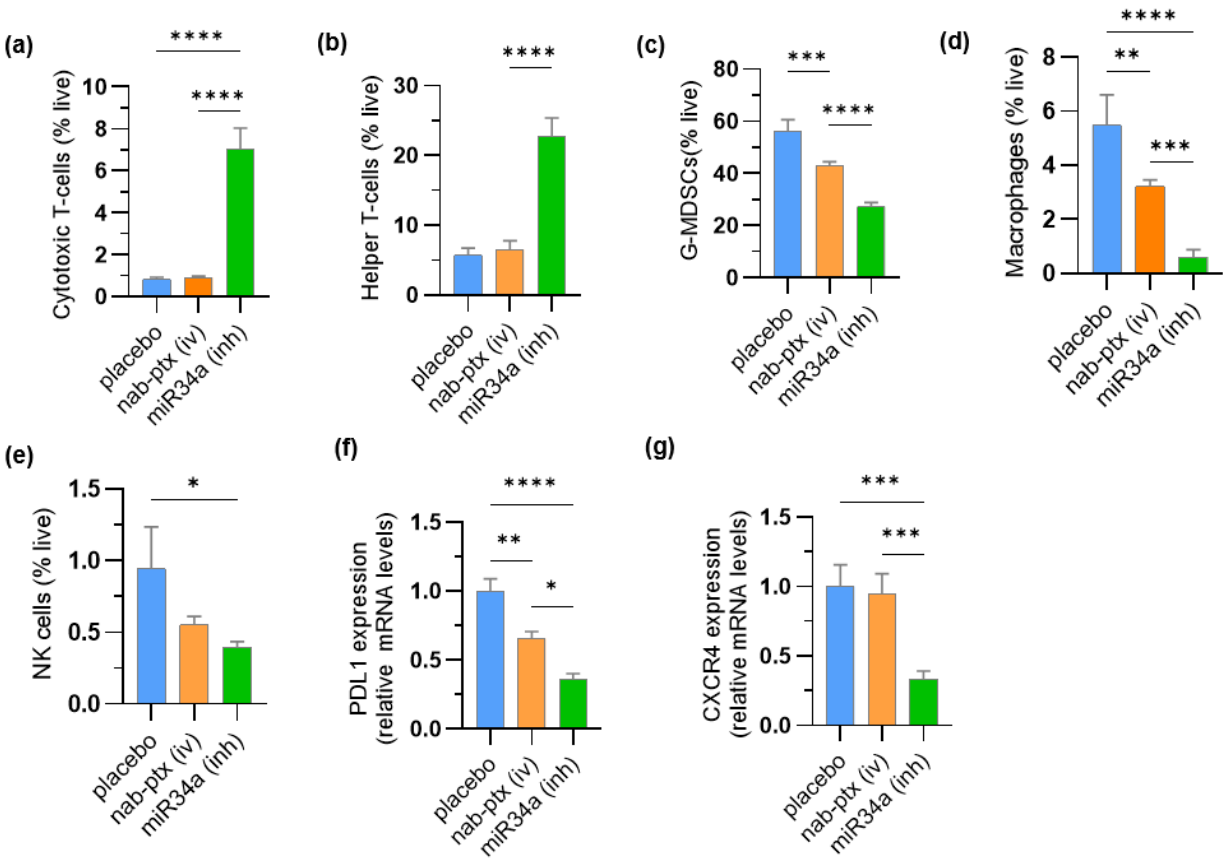

Figure 9. Effect of miR34a nanocapsule treatment on the levels of CD45+ cells in LMBC mice. Percentages of a) Cytotoxic T-cells, b) Helper T-cells, c) G-MDSCs, d) Macrophages, e) NK cells. Pulmonary mRNA levels of f) PDL1 and g) CXCR4. GAPDH was used as an internal control. n = 3, **** $p < 0.0001$, *** $p < 0.001$, ** $p < 0.01$, * $p < 0.05$

2.9 AAMD simulations to model the self-assembly of PAMD-C@PFOB particles in the presence of various excipients

While the nanocapsules are effective in delivering RNA to the lungs, our data show some particle agglomeration over time (Figure 2i). To study the impact of excipient molecules on particle agglomeration, AAMD simulations were performed for various systems. Since the actual particle sizes of ~170 nm are beyond the scope of AAMD simulations, the impact of excipients was modeled as a self-assembly problem. PFOB was approximated using 1-fluorobutane since the CHARMM force field was not directly available for fully fluorinated alkanes. As illustrated in **Figure 10a**, the initial configuration was generated using a random dispersion of PAMD-C molecules and 1-fluobutane molecules in water. This is denoted as the 'bare' system, without any excipients. For the 13 excipients modeled here (benzalkonium, citric acid, glucose, lactose, leucine, mannose, oleic acid, PEG400, polysorbate80, stearate, sucrose, trehalose, and vitamin E), the excipient molecules were also randomly placed in the simulation cell. Figure 10 b shows the simulation snapshots after 45 ns for few representative systems. The 'bare' system self-assembles to form a nearly spherical particle with a ~2.5 nm radius. Most 1-fluorobutane molecules (>99.5%, yellow) assemble to form the core and all PAMD-C molecules (purple) are deposited on the core. Upon adding stearate/oleic acid, the excipient molecules (green) are bound to the core particle. In contrast, mannose/sucrose molecules are randomly dispersed in the simulation cell and show very weak interactions with the core particle. To examine the structural integrity of the particles, the radius of gyration (k) was calculated for sub-structures and is summarized in Figure 10 c. When only 1-fluorobutane molecules are included, the value of k varies between 18-21 Å for all cases (bare system and the 13 excipients), indicating that the 1-fluorobutane molecules strongly interact with each other to form the core structure in all cases. When 1-fluorobutane and PAMD-C molecules are included, the value of k increases for all systems, as expected from the snapshots. When 1-fluorobutane, PAMD-C, and excipient molecules are included, the change in k can be used to infer the binding tendency of the excipient molecules. For benzalkonium, oleic acid, PEG400, polysorbate80, stearate, and vitamin E, the change in k (difference between the △ and □ markers) is small, indicating that the excipient molecules are strongly bound to the particle. In contrast the large change in k for citric acid, glucose, lactose, leucine, mannose, sucrose, and trehalose confirms that these molecules are randomly dispersed.

Further, clustering analysis presented in Figure 10 (d,e) shows the qualitative differences between the two sets of excipients. The number of clusters for excipients in Figure 10 d is

comparable to the number of clusters in the bare system (10-15), implying that these excipient molecules are bound to the particle. On the other hand, number of clusters varies between 20-60 for the excipients in Figure 10 e. Inspecting the snapshots in Figure 10 b shows that few 1-fluorobutane molecules are not part of the spherical core and are randomly dispersed. While these individual molecules contribute to the cluster count in Figure 10 (d,e) , they do not inhibit the tendency of the excipient to bind to the particle. Counting the percentage of bound/unbound excipient molecules directly correlates with its efficacy. Figure 10 f shows that the % unbound excipient molecules upon adding oleic acid, polysorbate80, stearate, and vitamin E is 0 (same as the bare system which does not have any excipients), confirming that all excipient molecules are bound the particle and the additional clusters in Figure 10 d correspond to the stray 1-fluorobutane molecules. Other excipients in Figure 10 g have large % unbound values. Lastly, Figure 10 (h, i) show the cumulative normalized histograms for Δr. For each PAMD-C or excipient molecule i, $\Delta r_i = \left\| r_i^{\mathrm{COM}} - r_{\mathrm{core}}^{\mathrm{COM}} \right\|$ is the Euclidean distance, where r_i^{COM} is the COM of the ith molecule and $r_{\mathrm{core}}^{\mathrm{COM}}$ is the COM of all 1-fluorobutane molecules (which form the core) in the system. This calculation is done at each time t in the simulation. Figure 10 h shows examples for stearate and oleic acid. In both cases, the dashed and solid histograms (calculation of Δr for PAMD-C and excipient molecules respectively) are close to each other, which convey that the PAMD-C and excipient molecules are at comparable radial distances from $r_{\mathrm{core}}^{\mathrm{COM}}$. In other words, stearate and oleic acid bind strongly to the particle. On the other hand, the separation between the dashed and solid histograms for mannose and sucrose is much larger (Figure 10 i), and indicate the weak interactions between the excipients and the particle. Additionally, the snapshots for mannose and sucrose in Figure 10 b show interactions between the particle and its periodic image. Such interactions are reduced for systems containing stearate, oleic acid, or other strong excipients, after stabilization of the particle (>30 ns). This suggests that weak excipients (such as mannose, sucrose, etc.) may not inhibit particle agglomeration. However, strong excipients may prevent or delay the agglomeration of neighboring particles, as supported by previous simulations for solid hydride particles[88-90]. Future work would be targeted at performing large-scale simulations to allow for the self-assembly of multiple such particles and elucidate the impact of adding various excipients.

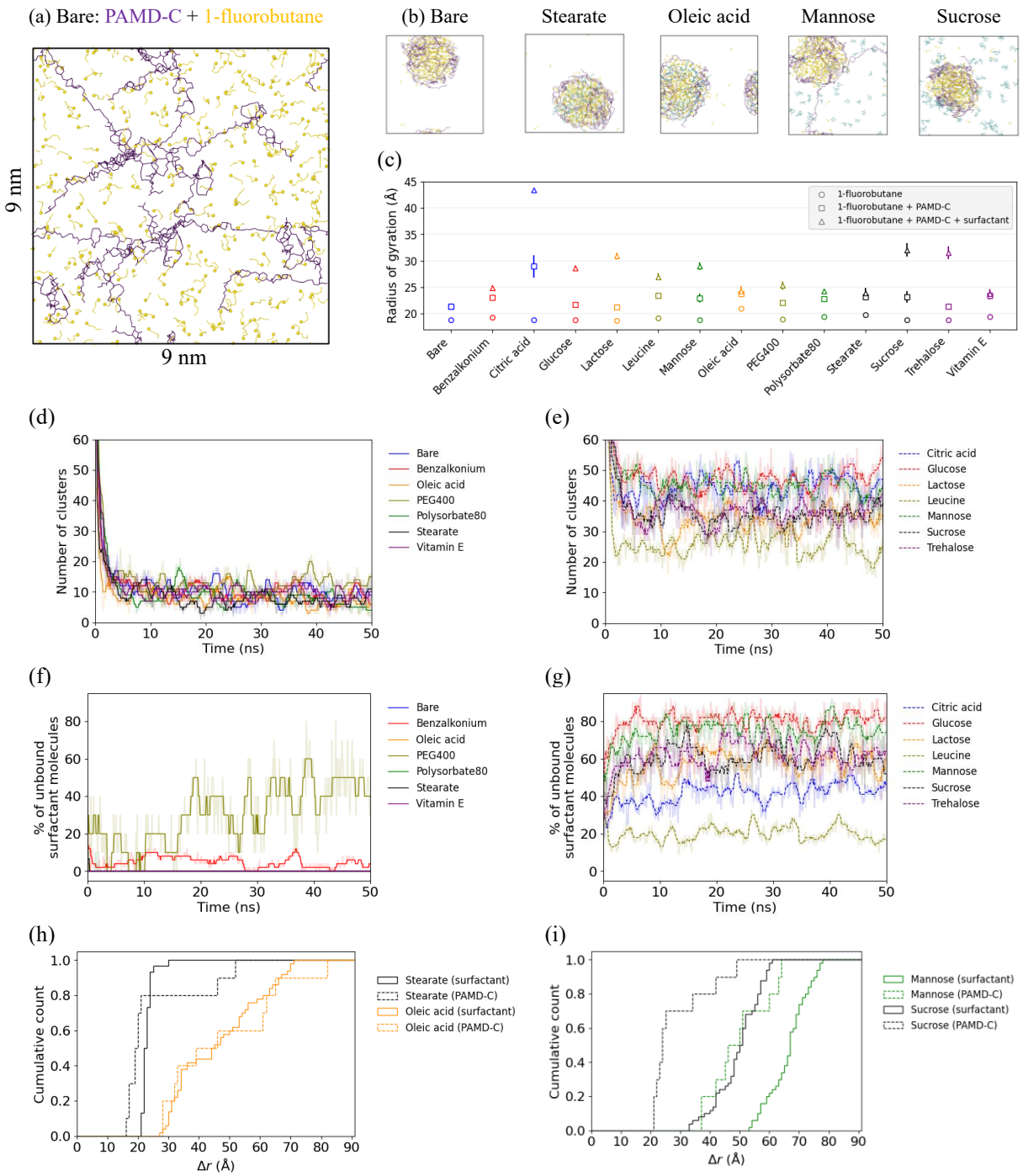

Figure 10: AAMD simulations to study self-assembly of PAMD-C@1-fluorobutane and various excipients. (a) Initial setup for the bare system containing PAMD-C and 1-fluorobutane. (b) Snapshots for various systems (PAMD-C + 1-fluorobutane + excipient) after 45 ns simulation. (c) Radius of gyration for all systems. There are three markers for each system representing the calculation of k using just the 1-fluorobutane molecules (○), 1-fluorobutane + PAMD-C molecules (□), and 1-fluorobutane + PAMD-C + excipient molecules (△). The vertical error bars denote the averaged value from 40-45 ns in the simulation. (d) and (e) show the evolution of number of clusters, (f) and (g) show the evolution of the % of excipient molecules bound to the core 1-fluorobutane + PAMD-C particle. In (d-g), the solid lines are obtained after median filtering and the shaded regions denote the raw output data. (h) and (i) show the cumulative normalized histogram for Δr (defined in the text). The distribution of Δr is calculated between 40 ns and 45 ns (100 ps interval) and averaged to generate the plots.

3. Conclusion

In conclusion, we have developed inhalable PFC-based nanocapsule, stabilized with an in-house developed polymeric surfactant, PAMD-C, for the targeted delivery of miRNA therapeutics to lung tumors. Our platform achieves an optimal aerodynamic diameter of ~1-2 μm for deep lung delivery, enabling efficient miRNA delivery to both healthy lung epithelial and tumor cells. Biodistribution studies confirm localized delivery to the mice lung with negligible accumulation in other organs, while demonstrating negligible immune-mediated clearance and significantly extended tumor retention time (> 48 h). The favorable safety profile of the RNA nanocapsule is evidenced by minimal inflammatory response, with only two cytokines (CXCL1 and TIMP-1) showing upregulation in healthy mice. The therapeutic efficacy of these nanocapsules encapsulating miR34a is demonstrated through potent pulmonary downregulation of PDL1 and CXCR4, markedly improved reduction in lung metastatic tumor burden (revealed by various histological analyses), and nearly doubled lifespan compared to standard chemotherapy after just three doses over two weeks. Furthermore, our delivery platform shows enhanced immunotherapy responses in the tumor microenvironment, overcoming many limitations of current chemotherapeutic approaches. These results provide clear evidence that stabilizing PFCs with cationic polymers like PAMD-C containing a CXCR4 targeting ligand leads to excellent tumor targeting ability, enabling effective delivery of RNAi therapeutics through inhalation. This approach successfully addresses common limitations in pulmonary inhalation therapy, such as poor cellular uptake, immune clearance of nanoparticles, and potential toxicity. Additionally, AAMD simulations indicate that excipients such as oleic acid, stearate, and vitamin E bind strongly with the nanocapsules and could potentially inhibit agglomeration and enhance the shelf-life of these formulations. Future work will be aimed at enhancing the structural stability of these formulations by using promising excipients identified from our AAMD simulations. With further optimization and testing of improved excipients, PFC-based nanocapsules may offer a translatable delivery strategy for global gene regulation in lung tumors and potentially other lung pathologies. Our study underscores the promise of PFCs as a versatile and effective platform for pulmonary-specific therapeutic interventions, presenting a new non-invasive platform for RNA delivery with enhanced therapeutic performance.

4. Experimental Section

Materials: All cell culture materials were obtained from Thermo Fisher Scientific, including Roswell Park Memorial Institute-1640 (RPMI-1640, catalog #11875093), Phosphate Buffered Saline (PBS, catalog #10010023), Fetal Bovine Serum (FBS), trypsin, penicillin, and streptomycin. Chemical reagents were sourced as follows: hexamethylenebisacrylamide (HMBA) from Pfaltz & Bauer (Waterbury, CT); 1-bromoheptadecafluorooctane (perfluorooctyl bromide , PFOB), N,N-diisopropylethylamine (DIPEA), heparin sodium salt (CAS #9041-08-1, catalog #H3149), and Cholesteryl chloroformate from Sigma-Aldrich (St. Louis, MO); and AMD3100 from A2B Chem LLC (catalog #AD67785). Nucleic acid reagents were acquired from various suppliers: negative control miRNA (miScr), carboxyfluorescein (FAM)- and Cy5.5-labeled miRNA, and microRNA 34a (mmu-miR-34a-5p) from Horizon Discovery. Cy3-NHS was procured from Lumiprobe Corporation (catalog #21020). The Proteome Profiler Mouse Cytokine Array Kit, Panel A (catalog #ARY006) was purchased from R&D Systems. Reverse-transcription PCR primers were obtained from Sigma-Aldrich and Sino-Biological Inc. Antibodies for immunophenotyping were sourced from BD Biosciences, BioLegend, and ThermoFisher Scientific.

Synthesis of PAMD-Cholesterol@PFOB nanoemulsions: Polymeric AMD3100 (PAMD) was synthesized via Michael-type addition using equimolar concentrations (1.9 mmol) of AMD3100 and HMBA as previously described [45]. The reactants were dissolved in methanol/water (7/3 v/v) and reacted at 37°C under nitrogen for 4 days in darkness. Subsequently, an additional one-tenth of the initial AMD3100 quantity was added and reacted for another day to consume any unreacted acrylamide. The reaction mixture was purified by dialysis (3.5 kDa MWCO) against methanol for 2 days, followed by dialysis against deionized water for an additional day. The final product was obtained by lyophilization at 38% yield. PAMD structure was confirmed by ^{1}H-NMR (Fig. S1), and molecular weight was determined by gel permeation chromatography (GPC) using an Agilent 1260 Infinity LC system with a TSKgel G2000PWXL-CP column in 0.1 M sodium acetate buffer (pH 5).

PAMD-Cholesterol (PAMD-C) was synthesized with 17% cholesterol substitution(Table S1). PAMD (310 mg) was dissolved in anhydrous methylene chloride (10 mL) with DIPEA (242.58 mg), and cholesteryl chloroformate (68.18 mg) in anhydrous methylene chloride was added dropwise over 1 hour on ice. The reaction proceeded for an additional 24 hours under stirring. The product was obtained by solvent evaporation and washed three times with diethyl ether to remove unreacted cholesteryl chloroformate. The product was then dissolved in ethanol/water

(1:1 v/v), and the pH was adjusted to 4.0 using 1.25 M HCl. Following dialysis (3.5 kDa MWCO) against ethanol/water (1:1 v/v) for 2 days and deionized(DI) water for 1 day, the product was lyophilized (85% yield). PAMD-C structure was confirmed using ^{1}H-NMR (Fig. S2). The intensity of integration of the cholesterol methyl group to the aromatic phenylene protons of PAMD was used for determining mol% and weight% of cholesterol in PAMD-C (Fig. S2, Table S3). The molecular weight of PAMD-C was determined using GPC (Table S1). Fluorescently labeled polymers were synthesized by reacting PAMD-C with Cy3-NHS ester (1% w/w) for 24 h at 40°C in darkness, followed by dialysis against distilled water for one day and lyophilization. PAMD-C@PFOB nanoemulsions were formulated by adding 20 µL PFOB to 2 mL PAMD-C (2 mg/mL in DI water) and ultrasonicating using a probe-type ultrasonic processor (Hielscher, UP200ST) equipped with a 2 mm diameter probe, with energy restricted to 8000 W at 80% output amplitude.

RNA nanocapsule preparation and characterization: RNA nanocapsules were formulated by mixing PAMD-C@PFOB nanoemulsions with 0.5 µg miRNA at different weight-to-weight (w/w) ratios of the PAMD-C polymer and miRNA in 10 mM HEPES buffer (pH 7.4) followed by incubation at room temperature for 30 min. The binding of miRNA to PAMD-C@PFOB was analyzed by a gel retardation assay. Nanocapsules prepared at different PAMD-C@PFOB to miRNA w/w ratios were loaded into the wells of a 2% agarose gel containing a SYBR™ Safe dye, which binds to unencapsulated miRNA. Gel electrophoresis was performed for 15 min at 100 mV in 0.5x Tris/borate/EDTA buffer. miRNA encapsulation was visualized using an E-Gel™ Imager (Invitrogen). The zeta potential and hydrodynamic diameter of the RNA nanocapsules were determined by dynamic light scattering (DLS) using the Zetasizer (Malvern Pananalytical). Nanocapsule morphology was examined by Transmission electron microscopy (TEM) using Nanovan® (Nanoprobes, catalog #2011) as a negative stain as well as by Cryo-TEM.

Aerosolization: Two aerosol generation systems were tested — microsprayer aerosolizer (PenWu Device for Mouse, BioJane, Cat# BJ-PW-M) and Aeroneb® Lab Nebulizer Small VMD (Kent Scientific Corporation, Cat# NEB-1100). For aerosol characterization, the RNA nanocapsules were prepared with 20µg miRNA and 80µg PAMD-C polymer(at w/w 4 from 2 mg/mL stock) and diluted in DI water in a ratio of 1:5 for aerosolization purposes as dilution led to lesser aggregation of the particles during aerosolization. For animal studies, the RNA nanocapsules were administered undiluted through the microsprayer.

Characterization of aerosolized RNA nanocapsules: To probe the aerodynamic size, the nanocapsules were aerosolized in an upwelling flow chamber, with an Aerodynamic Particle Sizer (APS) and a Next Generation Impactor (NGI) connected to the sample port. The upwelling vacuum flow rate was set at 50 L/min, and the flow rate leaving the side sampling port flow rate was set at 16 L/min. The APS sampled at 1 L/min while the NGI sampled at 15 L/min . The vacuum pulled for a total of 20 min, including a background sample for 10 min and a sample collection following aerosolization for another 10 min. The samples were aerosolized up to 1 minute for AeroNeb lab nebulizer or burst of aerosols from microsprayer aerosolizer and recorded for 10 minutes. APS (model 3321, TSI, Shoreview, MN, USA) was used to assess aerosol size and concentration. APS data was recorded on a connected laptop that used the Aerosol Instrument Management (v.10.3) software (TSI Inc., Shoreview, MN, USA).

NGI (MSP, Shoreview, Minn, USA) was used to determine the size of the collected particles. This NGI consists of 8 collection cups with the following size range cut-offs in um: 14.10, 8.61, 5.39, 3.30, 2.08, 1.36, 0.98 based on a sampling flow rate of 15 L/min [91]. Following each experimental run, impacted particles in the collection cups were rinsed with 10 mL of deionized water, and 200 µL was collected in a Qubit assay tube for fluorometry testing.

Aerosol Size and Quantification: To determine impacted particle size and quantity, Cy3 labelled PAMD-C@PFOB nanoemulsion was used. Following the sampling timeframe, fluorescent quantification was done with the Qubit 4 Fluorometer (Q33226, Invitrogen by Thermo Fisher Scientific, Wilmington, DE, USA). The fluorometer's green emission spectra (510 -580 nm) were used based on the excitation peak of Cy3~ 554nm to calculate the relative fluorescence units (RFU). Emission readings were entered into Excel for analysis. The R^2 values and slope of the curve were used to determine the fluorescein concentration in mg/mL. The RFU values were fit to the curve using the following equation: $y = 30030x + 2609.2$; $R^2 = 0.9606$

Cell culture: 4T1-Luc [Ubigene] (RRID: CVCL_C8UY) and NCI-H1975-Luc [Ubigene] (RRID: CVCL_C8W1) cell lines were obtained on January 2021 and March 2022 respectively. Cells were cultured in RPMI-1640 media with 10% FBS and 1% penicillin-streptomycin. 4T1-Luc-mCherry cells (RRID: CVCL_C8UZ) were a kind gift from Dr. Shyamala Maheswaran from Massachusetts General Hospital Harvard University in June, 2024 and they were cultured in Gibco RPMI-1640 (A10491-01) (ATCC modification 30-2001) with 10% FBS and 1%

penicillin-streptomycin. Recombinant human osteosarcoma epithelial cells U2OS expressing EGFP-tagged CXCR4 receptor was obtained in October, 2018 from Thermo Fisher, USA (#K1779, RRID:CVCL_ZK12) and were cultured in DMEM high glucose medium supplemented with 10% FBS, 2 mM L-Glutamine, 1% Penicillin-Streptomycin and 0.5 mg/mL G418. Cells were cultured in a humidified incubator at 37 °C with 5% CO_2.

In vitro cytotoxicity: In vitro cytotoxicity of nanoemulsions and nanocapsules was assessed by CellTitre-Blue (CTB) cell viability assay (Promega, catalog # G8080). 4T1-Luc and H1975-Luc cells were seeded in 96-well plates at a density of 10,000 cells/well and incubated overnight. The next day, cells were treated with increasing concentrations of the nanoemulsion and nanocapsules (formulated with increasing concentrations of miRNA) and incubated for 24 h. Then, cell viability was evaluated by CTB assay following the manufacturer's protocol. The half maximal inhibitory concentration (IC_{50}) values were calculated from a dose-response analysis in GraphPad Prism.

Luciferase gene silencing by aerosolized RNA nanocapsules in vitro: 4T1.Luc cells were seeded in a 48-well plate at a density of 3×10^4 cells per well and incubated overnight. RNA nanocapsules (PAMD-C@PFOB/siLuc) containing siLuc(*Silencer*™ Firefly Luciferase (GL2 + GL3) siRNA , Thermo Fisher, Cat# AM4629) or negative control siRNA at w/w 4, 150 nM siRNA per well, were prepared and subjected to aerosolization using the Aeroneb lab nebulizer and the microsprayer aerosolizer. Both pre- and post-aerosolized RNA nanocapsules were then used to transfect the cells in serum-free medium for 6 hours. Following transfection, the medium was replaced with fresh medium containing 10% FBS and kept for 48 hours. Subsequently, cells were washed with PBS, lysed using cell lysis buffer, and luciferase activity was quantified using the Promega Luciferase Assay System (Cat. No. E1500).

CXCR4 inhibition assay: CXCR4 inhibitory activity by PAMD-C@PFOB was assessed by CXCR4-redistribution assay in U2OS cells stably expressing EGFP-bound CXCR4 receptor as reported in previous studies[92]. U2OS cells were seeded in black clear-bottomed 96 well plates at a density of 15,000 cells/well and incubated overnight. Next day, the cells were washed twice with 100 μL of assay buffer and incubated with increasing concentrations of PAMD-C@PFOB nanoemulsion for 30 mins. Next, 10 nM of stromal cell-derived factor 1 (SDF-1, Millipore Sigma Catalog # GF344) was added to the cells followed by incubation for 1 h. The cells were fixed with 10% formalin for 20 mins followed by three washes with PBS and then

visualized using a fluorescence microscope (EVOS® FL). CXCR4 receptor internalization was measured via a Cellomics ArrayScan V high-content analysis plate reader, which detected fluorescent spots formed when CXCR4-EGFP fusion proteins moved into endosomes. Here, SDF-1 functioned as the agonist, while the CXCR4-specific inhibitor AMD3100 was used as a reference antagonist.

Intracellular localization and quantification of cellular uptake of the nanocapsules: To assess subcellular localization of the RNA nanocapsules via confocal microscopy, 4T1-Luc cells were plated on 15 mm glass-bottomed cell culture dishes overnight at a density of 10,000 cells/well. Next day, cells were transfected with nanocapsules prepared using Cy3-labelled PAMD-C@PFOB and FITC-labelled miRNA (w/w 4, 150 nM miRNA) for 6 h. Cells were washed thrice with PBS, and the nuclei were stained with 4′,6-diamidino-2-phenylindole (DAPI). Finally, cells were fixed using 10% formalin before imaging on a confocal microscope (Zeiss LSM 800 with Airyscan). For quantification of uptake of the labelled RNA nanocapsules using flow cytometry, 4T1-Luc cells were seeded in 6-well plates overnight and the above-mentioned treatments were given the next day for 6 h. Cells were then washed thrice with PBS, detached with TrypLE (Gibco), and analyzed by flow cytometry on a FACSCalibur instrument (BD Biosciences). Free FITC labelled miRNA was used as a control.

Animal models of lung metastatic breast cancer (LMBC) : All animal experiments were conducted using 8-week-old female Balb/c mice obtained from Charles River Laboratories. All experiments were performed according to an approved protocol by the Institutional Animal Care and Use Committee(IACUC) having protocol no 19-018-03FC of the University of Nebraska Medical Center. The LMBC model was established by tail vein injection of $2x10^5$ 4T1-Luc-mCherry cells in 100 µl sterile PBS per mouse. This modified cell line was used to track metastasis and tumor progression through both bioluminescent imaging (via the luciferase protein expression) and fluorescent visualization (via mCherry protein expression). LMBC model using the 4T1 cells (a highly metastatic mammary cancer cell line) serves as a model for stage IV human breast cancer. Studies show that mice implanted with 4T1 cells developed progressively growing tumors that spontaneously metastasized to the lungs, ultimately resulting in death from metastatic disease in all animals [93]. The lung metastasis was confirmed at different days post implantation starting at day 5, by IVIS bioluminescence imaging after intraperitoneal injection of Luciferin substrate (3 mg per mouse). The mice were provided with a standard diet and had unrestricted access to water.

Biodistribution of RNA nanocapsules: Biodistribution was assessed in healthy and LMBC mice model at different time points post administration of nanocapsules. On day 12, post tumor implantation, lung metastasis was confirmed by *in vivo* bioluminescence imaging. Then the microsprayer aerosolizer was used to administer aerosolized RNA nanocapules (60 µL) formulated with Cy3- labelled PAMD-C@PFOB and Cy5.5-labelled miRNA(Dharmacon) (20 µg miRNA per mouse, w/w=4) in mice (n=3 per group). Mice were euthanized at different times (6 h, 12 h, 24 h and 48 h) post administration of the nanocapsules and major organs were collected for *ex vivo* imaging on a Xenogen IVIS 200 system.

Intra-pulmonary distribution of labelled RNA nanocapsules in healthy and LMBC mice: On day 12, lung metastasis was confirmed in LMBC mice by *in vivo* imaging on a Xenogen IVIS 200 system detecting fluorescence from mcherry cells. Then mice in the healthy as well as LMBC group received an equivalent volume of the labelled nanocapsules as mentioned above. To assess intra-pulmonary distribution of the nanocapsules, lungs were perfused and embedded in Tissue-Tek® optimal cutting temperature (O.C.T.) Compound (Sakura® Finetek Catalog # 4583), sectioned, stained with DAPI, and then fluorescence from Cy3, Cy5.5 and mcherry was visualized on a Zeiss Axioscan 7 microscope.

In vivo therapeutic efficacy: The therapeutic efficacy of RNA nanocapsules was evaluated in LMBC model. Mice were randomly assigned to three treatment groups (n=15 per group): (1) Placebo receiving saline (i.v.) and DI water (aerosol), (2) NAB Paclitaxel (i.v.), (3) aerosolized PAMD-C@PFOB/miR34a. NAB-Paclitaxel was administered intravenously on days 5 and 9 at a dose of 10 mg/kg body weight in 100 µL sterile PBS, totaling two doses. RNA nanocapsule treatments were administered intratracheally using a microsprayer aerosolizer (PenWu, BioJane) on days 6, 10, and 14, totaling 3 doses. Each nanocapsule dose consisted of 20 µg miR34a formulated with PAMD-C@PFOB nanoemulsion (w/w 4) and 10% 10 mM HEPES in a total volume of 60 µL. Body weights were recorded throughout the study. On day 16, three mice per group were injected intraperitoneally with 3 mg D-luciferin in 100 µL PBS for bioluminescence imaging to assess tumor burden. Five mice from each group were monitored for survival until day 53 without any additional treatment. On day 16, multiple analyses were performed: four mice per group were sacrificed for flow cytometric analysis of the tumor immune microenvironment using lung single-cell suspensions; three mice per group were used for RNA extraction from lung tissue to confirm relative mRNA levels of PDL1, a target of

miR34a , via RT-PCR; and the remaining three mice per group had their lungs perfused with formalin fixed in 4% paraformaldehyde for 24 hours, embedded in paraffin, and sectioned for H&E and IHC staining.

Pulmonary single cell isolation and flow cytometry analysis of nanocapsule uptake: We employed flow cytometry to quantify the uptake of Cy5.5-labelled miRNA in mouse lung epithelial, endothelial, and hematopoietic lineage cells. Additionally, this method also allowed us to assess immunomodulation within the lung tissue following various treatments.

Epithelial & endothelial cell (CD45-) isolation: At the time of lung tissue harvest, the pulmonary circulation was flushed by injecting 10 mL of cold 1x PBS containing 500 U/mL heparin(150 µL from 10,000 u/ml) through the left ventricle of the heart. The lung was inflated with 1.5 mL cold Dispase solution (Corning, Catalog # 354235) by instilling a catheter through the trachea. This was followed by perfusion with 200 µL of 1% low melting point (LMP) agarose (CAS# 9012-36-6, GoldBio). The lungs were immediately placed in ice and incubated for 2 min, followed by incubation for 45 minutes in 5 mL of Hank's Balanced Salt Solution without Calcium and Magnesium (HBSS) (Thermo Fisher, Catalog # 14175095) at room temperature. The lungs were minced using scissors and transferred to a gentleMACS™ C tube (Miltenyi Biotec Catalog # 130-093-237) containing 1 mL of Dulbecco's Modified Eagle Medium (DMEM) and 100 µL of 1 mg/mL DNase I (Sigma-Aldrich, Catalog # 11284932001).

CD45+ cell isolation: Collagenase Type IV (Sigma, CAS #9001-12-1) was prepared at a concentration of 700 mg per 500 mL of Dulbecco's Modified Eagle Medium (DMEM). Following the pulmonary circulation flushing procedure described previously, the lungs were minced using scissors and transferred to a gentleMACS™ C tube. Each tube contained 1 mL of the prepared DMEM with Collagenase IV, 100 µL of DNase I (1 mg/mL), and 30 µL of Heparin (from 10,000 U/mL).

The C tubes were placed upside down in the gentleMACS™ Dissociator (Miltenyi Biotec, Catalog # 130-093-235) and the tissue was dissociated for 8 seconds to form a single cell suspension, which was immediately transferred to ice. An additional 4 mL of DMEM was added, and the tubes were kept in a rotating incubator at 150 rpm for 30 minutes at 37°C. Then added 5 mL of 1x PBS containing 4 mM EDTA at pH 7.4 (Teknova Catalog # P0203) and the cells were sequentially filtered through pre-separation filters of 70 µm (Miltenyi Biotec, Catalog # 130-095-823) and 40 µm (Corning Cat # 352340). The cell suspension was centrifuged at 1500

rpm for 10 minutes. After decanting the supernatant, 1 mL of ACK Lysis Buffer (Quality Biological, Catalog # 118-156-721) was added to the cells and vortexed gently to lyse the RBCs. This mixture was kept for 2 minutes, after which 2 mL of DMEM was added. It was again vortexed gently, and the cells were centrifuged at 1500 rpm for 5 minutes. The supernatant was decanted, and the cells were resuspended in 500 µL of FACS Buffer (1X PBS + 2% FBS + 0.1% NaN_3). The cells were counted in the TC10™ automated cell counter and the antibodies used for the flow cytometry staining are shown in Table S2. The gating strategy used to separate the pulmonary immune and epithelial/endothelial cells as well for immunophenotyping in the therapeutic study are shown in Figure S6 and Figure S7 , respectively.

Cytokine Array: To assess inflammation in lung tissue post administration of the RNA nanocapsules, a cytokine array was conducted in 8-week-old female Balb/c healthy mice. The study included three groups: one receiving aerosolized PAMD-C@PFOB/miRNA nanocapsules, a healthy control group, and a placebo control group receiving aerosolized DI water. Twelve hours after administering the formulations, lungs were harvested, protein lysates prepared by homogenizing the lung tissue in RIPA lysis buffer containing protease and phosphatase inhibitor cocktails (Thermo Fisher Scientific). Protein concentration was determined using the Bradford reagent. Approximately 300 µg of pooled protein extract from lung tissue was used for cytokine quantification. The antibody-based protein array (Proteome Profiler: Mouse Cytokine Array, R&D Systems, catalog number: ARY006) was employed according to the manufacturer's instructions. Densitometry of cytokine spots on the membrane was performed using Image Lab 6.1 software (Bio-Rad) with the volumetric method to determine cytokine expression levels after background subtraction.

Reverse transcription–polymerase chain reaction (RT-PCR): Total RNA was extracted from lung tissues using TRIzol reagent (Invitrogen #15596026). The RNA was then converted to cDNA using a high-capacity reverse transcription kit from Applied Biosciences (#43-688-14). RT-PCR analysis was conducted on a Roto-Gene Q (Qiagen) thermocycler using a iTaq Universal SYBR Green Super mix (Bio-Rad #1725121) following the manufacturer's protocol. Relative mRNA levels were calculated using the Ct values obtained. All primer sequences used are listed in Table S3.

Histological analysis: Mouse lung tissues from the different treatment groups were perfused and fixed in 4% paraformaldehyde and then stored in 75% ethanol. Then the lung tissues were

embedded in paraffin, sectioned and stained with hematoxylin and eosin (H&E) using standard protocols. For immunohistochemistry (IHC), antigen retrieval was performed on the tissue sections by immersing them in heated citrate buffer (pH 6.0) for 20 min. 3% hydrogen peroxide was used to block endogenous peroxidase activity, followed by incubation in 5% normal goat serum to prevent non-specific binding. The tissue sections were then incubated at 4°C overnight with primary antibodies, followed by 1 h incubation at room temperature with HRP-conjugated secondary antibody. All slides were imaged using a Leica Aperio CS2 scanning system and images were analyzed using a Aperio Image Scope Software (Leica Biosystems).

Molecular Dynamics (MD) Simulations: Interaction potentials for all molecules in this study were parametrized using the CHARMM code [94-96]. PFOB was approximated using 1-fluorobutane since the CHARMM force field was not directly available for fully fluorinated alkanes. All-atom molecular dynamics (AAMD) simulations were run using the GROMACS code [97]. Input configurations (9 nm × 9 nm × 9 nm) were generated using CHARMM-GUI [94, 96]. All systems were neutralized at a pH of 7 using Na+ and Cl- ions. AAMD simulations were run for 50 ns (2 fs timestep) in the NPT ensemble at 303.15 K and 1 bar. Snapshots were saved every 100 ps. Details for each system including number of molecules and their structure are shown in the Table S4, Supplementary Information. Visualization and clustering analysis was done using OVITO [98].

Statistical analysis: Results are presented as mean ± standard deviation. Statistical differences between three or more groups were analyzed using one-way ANOVA with Tukey's post-hoc test, while Student's t-test was employed for analyzing differences between two groups. Survival curves were analyzed using the log-rank test. A p-value < 0.05 was considered statistically significant, and all statistical analyses were conducted using GraphPad Prism 9.

Acknowledgements

This research was supported by funds from the University of Nebraska Medical Center and grants P30 GM127200, R01 CA235863, R01 DK120533, and R01 DK124095. We gratefully acknowledge the University of Nebraska Medical Center's Advanced Microscopy Core Facility, Flow Cytometry Core Facility, and Tissue Sciences Core Facility for their support. We would also like to thank Holly C. Britton, Dr. Craig L. Semerad, Amy J. Nelson, and Dr. Sudipta Panja, for their contributions to this work. The Core Facility receives partial support from NIGMS INBRE (P20 GM103427) and COBRE (P30 GM106397) grants, as well as support

from NCI for The Fred & Pamela Buffett Cancer Center Support Grant (P30 CA036727). Major instrumentation has been provided by the Office of the Vice Chancellor for Research, The University of Nebraska Foundation, the Nebraska Banker's Fund, and by the NIH-NCRR Shared Instrument Program. The content and interpretations presented in this publication are solely the responsibility of the authors.

Conflict of Interest

The authors declare no conflict of interest.

Data Availability Statement

The data that support the findings of this study are available from the corresponding author upon reasonable request.

References

[1] N. Motas, M. D. Davidescu, B. C. Tanase, O. Rus, A. I. Burlacu, V. Alexe, V. Manolache, M. C. Mizea, N. Gheorghiu, O. G. Trifanescu, *Diagnostics* **2023**, *13* (1), 165.
[2] T. Martin, J. Moseley, *Endocrine-Related Cancer* **2000**, *7* (4), 271.
[3] S. Welter, J. Jacobs, T. Krbek, M. Tötsch, G. Stamatis, *European Journal of Cardio-Thoracic Surgery* **2008**, *34* (6), 1228.
[4] I. Godet, M. Mamo, A. Thurnheer, D. M. Rosen, D. M. Gilkes, *Cancers* **2021**, *13* (21), 5509.
[5] D. K. Filippiadis, E. Efthymiou, K. Palialexis, E. Brountzos, N. Kelekis, *Diagn Interv Radiol* **2022**, *28* (3), 249.
[6] J. Fan, D. Chen, H. Du, C. Shen, G. Che, *Journal of Thoracic Disease* **2015**, *7* (8), 1441.
[7] Y. Xu, A. Thakur, Y. Zhang, C. Foged, *Pharmaceutics* **2021**, *13* (2), 177.
[8] N. K. Verma, K. Crosbie-Staunton, A. Satti, S. Gallagher, K. B. Ryan, T. Doody, C. McAtamney, R. MacLoughlin, P. Galvin, C. S. Burke, *Journal of Nanobiotechnology* **2013**, *11*, 1.
[9] K. Dua, R. Wadhwa, G. Singhvi, V. Rapalli, S. D. Shukla, M. D. Shastri, G. Gupta, S. Satija, M. Mehta, N. Khurana, *Drug development research* **2019**, *80* (6), 714.
[10] O. M. Merkel, T. Kissel, *Accounts of chemical research* **2012**, *45* (7), 961.
[11] N. R. Labiris, M. B. Dolovich, *British journal of clinical pharmacology* **2003**, *56* (6), 588.
[12] L. Ding, S. Tang, T. A. Wyatt, D. L. Knoell, D. Oupický, *Journal of controlled release* **2021**, *330*, 977.
[13] J. Kim, A. Jozic, Y. Lin, Y. Eygeris, E. Bloom, X. Tan, C. Acosta, K. D. MacDonald, K. D. Welsher, G. Sahay, *ACS nano* **2022**, *16* (9), 14792.
[14] A. Y. Jiang, J. Witten, I. O. Raji, F. Eweje, C. MacIsaac, S. Meng, F. A. Oladimeji, Y. Hu, R. S. Manan, R. Langer, *Nature nanotechnology* **2024**, *19* (3), 364.
[15] K. P. Friis, S. Gracin, S. Oag, A. Leijon, E. Sand, B. Lindberg, E. Lázaro-Ibáñez, J. Lindqvist, K. A. Whitehead, A. Bak, *Journal of Controlled Release* **2023**, *363*, 389.
[16] J. Kim, A. Jozić, E. Bloom, B. Jones, M. Marra, N. T. V. Murthy, Y. Eygeris, G. Sahay, *ACS nano* **2024**, *18* (17), 11335.

[17] W. Tao, X. Mao, J. P. Davide, B. Ng, M. Cai, P. A. Burke, A. B. Sachs, L. Sepp-Lorenzino, *Molecular Therapy* **2011**, *19* (3), 567.
[18] T. Nii, I. Takeuchi, Y. Kimura, K. Makino, *Colloids and Surfaces A: Physicochemical and Engineering Aspects* **2018**, *539*, 347.
[19] S. Mangal, W. Gao, T. Li, Q. T. Zhou, *Acta pharmacologica sinica* **2017**, *38* (6), 782.
[20] M. Moreno-Sastre, M. Pastor, C. J. Salomon, A. Esquisabel, J. Pedraz, *Journal of Antimicrobial Chemotherapy* **2015**, *70* (11), 2945.
[21] I. M. El-Sherbiny, N. M. El-Baz, M. H. Yacoub, *Global Cardiology Science and Practice* **2015**, *2015* (1), 2.
[22] Z. Zhang, C. Kleinstreuer, C. Kim, A. Hickey, *Inhalation Toxicology* **2002**, *14* (11), 1111.
[23] M. Amararathna, K. Goralski, D. W. Hoskin, H. V. Rupasinghe, *Journal of lung health and diseases* **2019**, *3* (2).
[24] J. G. Riess, M. P. Krafft, *Artificial Cells, Blood Substitutes, and Biotechnology* **1997**, *25* (1-2), 43.
[25] J. G. Riess, *Artificial cells, blood substitutes, and biotechnology* **2005**, *33* (1), 47.
[26] A. Das, R. Niven, *Journal of pharmaceutical sciences* **2001**, *90* (9), 1336.
[27] D. J. Weiss, T. P. Strandjord, D. Liggitt, J. G. Clark, *Human gene therapy* **1999**, *10* (14), 2287.
[28] D. A. Lisby, P. L. Ballard, W. W. Fox, M. R. Wolfson, T. H. Shaffer, L. W. Gonzales, *Human gene therapy* **1997**, *8* (8), 919.
[29] J. H. Modell, F. Gollan, S. T. Giammona, D. Parker, *Chest* **1970**, *57* (3), 263.
[30] T. F. Miller, B. Milestone, R. Stern, T. H. Shaffer, M. R. Wolfson, *Journal of Applied Physiology* **2001**, *90* (3), 839.
[31] C. A. Reickert, T. Pranikoff, M. C. Overbeck, E. A. Kazerooni, K. D. Massey, R. H. Bartlett, R. B. Hirschl, *Chest* **2001**, *119* (2), 515.
[32] M. Al-Saiedy, E. Nelson, T. El-Mays, M. Amrein, F. Green, Perflubron enhances mucin plug clearance in vitro in the presence of natural surfactant. European Respiratory Society: **2013**.
[33] X. Song, L. Feng, C. Liang, K. Yang, Z. Liu, *Nano letters* **2016**, *16* (10), 6145.
[34] Y. Yang, Y. Liu, Y. Jiang, *Molecular Pharmaceutics* **2023**, *20* (7), 3254.
[35] H.-J. Lehmler, *Expert review of respiratory medicine* **2008**, *2* (2), 273.
[36] U. Merz, B. Klosterhalfen, M. Häusler, M. Kellinghaus, T. Peschgens, H. Hörnchen, *Pediatric research* **2002**, *51* (2), 183.
[37] V. V. Obraztsov, G. G. Neslund, E. S. Kornbrust, S. F. Flaim, C. M. Woods, *American Journal of Physiology-Lung Cellular and Molecular Physiology* **2000**, *278* (5), L1018.
[38] J. Varani, R. B. Hirschl, M. Dame, K. Johnson, *Shock* **1996**, *6* (5), 339.
[39] A. Baba, Y. K. Kim, H. Zhang, M. Liu, A. S. Slutsky, *Critical care medicine* **2000**, *28* (4), 1113.
[40] S. Nakata, K. Yasui, T. Nakamura, N. Kubota, A. Baba, *Neonatology* **2007**, *91* (2), 127.
[41] T. Delmas, H. Piraux, A.-C. Couffin, I. Texier, F. Vinet, P. Poulin, M. E. Cates, J. Bibette, *Langmuir* **2011**, *27* (5), 1683.
[42] J. Li, D. Oupicky, *Biomaterials* **2014**, *35* (21), 5572, https://doi.org/10.1016/j.biomaterials.2014.03.047.
[43] Y. Wang, S. Kumar, S. Rachagani, B. R. Sajja, Y. Xie, Y. Hang, M. Jain, J. Li, M. D. Boska, S. K. Batra, D. Oupicky, *Biomaterials* **2016**, *101*, 108.
[44] Y. Xie, Y. Hang, Y. Wang, R. Sleightholm, D. R. Prajapati, J. Bader, A. Yu, W. Tang, L. Jaramillo, J. Li, R. K. Singh, D. Oupicky, *ACS Nano* **2020**, *14* (1), 255, https://doi.org/10.1021/acsnano.9b03978 [doi].
[45] Y. Wang, J. Li, Y. Chen, D. Oupický, *Biomaterials science* **2015**, *3* (7), 1114.

[46] Y. Hang, S. Tang, W. Tang, D. Vetvicka, C. Zhang, Y. Xie, F. Yu, A. Yu, D. Sil, J. Li, R. K. Singh, D. Oupicky, *J Control Release* **2021**, *333*, 139.
[47] D. Y. Furgeson, W. S. Chan, J. W. Yockman, S. W. Kim, *Bioconjugate chemistry* **2003**, *14* (4), 840.
[48] D.-a. Wang, A. S. Narang, M. Kotb, A. O. Gaber, D. D. Miller, S. W. Kim, R. I. Mahato, *Biomacromolecules* **2002**, *3* (6), 1197.
[49] X. Liang, M. Chen, P. Bhattarai, S. Hameed, Z. Dai, *ACS nano* **2020**, *14* (10), 13569.
[50] M. M. Lewis, M. R. Soto, E. Y. Maier, S. D. Wulfe, S. Bakheet, H. Obregon, D. Ghosh, *Bioengineering & translational medicine* **2023**, *8* (6), e10580.
[51] E. R. Sudduth, E. L. Kolewe, J. Graf, Y. Yu, J. Somma, C. A. Fromen, *Frontiers in chemical engineering* **2023**, *4*, 1086031.
[52] Y.-C. Kuo, T.-W. Lin, *The Journal of Physical Chemistry B* **2006**, *110* (5), 2202.
[53] M. M. Gaspar, O. Gobbo, C. Ehrhardt, *Journal of Liposome Research* **2010**, *20* (1), 55.
[54] A. Cochard, M. G.-J. Navarro, L. Piroska, S. Kashida, M. Kress, D. Weil, Z. Gueroui, *Biophysical Journal* **2022**, *121* (9), 1675.
[55] S. J. Eastman, J. D. Tousignant, M. J. Lukason, H. Murray, C. S. Siegel, P. Constantino, D. J. Harris, S. H. Cheng, R. K. Scheule, *Human gene therapy* **1997**, *8* (3), 313.
[56] L. Ding, S. Tang, W. Tang, D. D. Mosley, A. Yu, D. Sil, S. Romanova, K. L. Bailey, D. L. Knoell, T. A. Wyatt, *Advanced Science* **2022**, *9* (8), 2103676.
[57] H. Wang, X. Li, J. Wang, J. Wang, H. Zou, X. Hu, L. Yang, P. Shen, K. Wang, Y. Li, *Nano Letters* **2023**, *23* (7), 2964.
[58] B. Seubert, B. Grünwald, J. Kobuch, H. Cui, F. Schelter, S. Schaten, J. T. Siveke, N. H. Lim, H. Nagase, N. Simonavicius, *Hepatology* **2015**, *61* (1), 238.
[59] K.-C. Ngamsri, C. Jans, R. A. Putri, K. Schindler, J. Gamper-Tsigaras, C. Eggstein, D. Köhler, F. M. Konrad, *Frontiers in Immunology* **2020**, *11*, 407.
[60] R. Yumoto, H. Nishikawa, M. Okamoto, H. Katayama, J. Nagai, M. Takano, *American Journal of Physiology-Lung Cellular and Molecular Physiology* **2006**, *290* (5), L946.
[61] I. M. Adcock, E. Mortaz, S. D. Alipoor, J. Garssen, A. A. Velayati, *The International Journal of Mycobacteriology* **2016**, *5* (Suppl 1), S157.
[62] L. Möckl, S. Hirn, A. A. Torrano, B. Uhl, C. Bräuchle, F. Krombach, *Nanomedicine* **2017**, *12* (3), 207.
[63] Y. Liu, Y. He, H. Xu, A. Remmo, F. Wiekhorst, F. Heymann, H. Liu, E. Schellenberger, A. Häckel, R. Hauptmann, *Nano Letters* **2024**, *24* (49), 15607.
[64] P. H. Olivieri Jr, I. F. Assis, A. F. Lima, S. A. Hassan, R. J. Torquato, J. Y. Hayashi, A. K. Tashima, H. B. Nader, A. Salvati, G. Z. Justo, *ACS Applied Bio Materials* **2024**, *7* (11), 7365.
[65] L. Zhang, Y. Liao, L. Tang, *Journal of Experimental & Clinical Cancer Research* **2019**, *38*, 1.
[66] S. Deng, M. Wang, C. Wang, Y. Zeng, X. Qin, Y. Tan, B. Liang, Y. Cao, *Molecular Biology Reports* **2023**, *50* (1), 577.
[67] X. Wang, J. Li, K. Dong, F. Lin, M. Long, Y. Ouyang, J. Wei, X. Chen, Y. Weng, T. He, *Cellular signalling* **2015**, *27* (3), 443.
[68] I. X. Chen, V. P. Chauhan, J. Posada, M. R. Ng, M. W. Wu, P. Adstamongkonkul, P. Huang, N. Lindeman, R. Langer, R. K. Jain, *Proceedings of the National Academy of Sciences* **2019**, *116* (10), 4558.
[69] S. Hassan, M. Buchanan, K. Jahan, A. Aguilar‐Mahecha, L. Gaboury, W. J. Muller, Y. Alsawafi, A. A. Mourskaia, P. M. Siegel, O. Salvucci, *International journal of cancer* **2011**, *129* (1), 225.

[70] S. A. DuPré, D. Redelman, K. W. Hunter Jr, *International journal of experimental pathology* **2007**, *88* (5), 351.
[71] H.-H. Lin, D. E. Faunce, M. Stacey, A. Terajewicz, T. Nakamura, J. Zhang-Hoover, M. Kerley, M. L. Mucenski, S. Gordon, J. Stein-Streilein, *Journal of Experimental Medicine* **2005**, *201* (10), 1615.
[72] P. T. de Lara, H. Castañón, M. Sterpi, M. van den Broek, *Trends in cancer* **2022**, *8* (2), 145.
[73] Y. Zhang, H. C. Ertl, *Frontiers in immunology* **2016**, *7*, 32.
[74] H. Cheng, K. Ma, L. Zhang, G. Li, *Cancer letters* **2021**, *506*, 55.
[75] Y. D. Seo, X. Jiang, K. M. Sullivan, F. G. Jalikis, K. S. Smythe, A. Abbasi, M. Vignali, J. O. Park, S. K. Daniel, S. M. Pollack, *Clinical Cancer Research* **2019**, *25* (13), 3934.
[76] R. Bos, L. A. Sherman, *Cancer research* **2010**, *70* (21), 8368.
[77] K. H. Parker, D. W. Beury, S. Ostrand-Rosenberg, *Advances in cancer research* **2015**, *128*, 95.
[78] Y. Sun, X. Han, C. Shang, Y. Wang, B. Xu, S. Jiang, Y. Mo, D. Wang, Y. Ke, X. Zeng, *Cell Death & Disease* **2022**, *13* (1), 36.
[79] J. A. Park, L. Wang, N.-K. V. Cheung, *Journal of hematology & oncology* **2021**, *14*, 1.
[80] L. Sun, P. E. Clavijo, Y. Robbins, P. Patel, J. Friedman, S. Greene, R. Das, C. Silvin, C. Van Waes, L. A. Horn, *JCI insight* **2019**, *4* (7), e126853.
[81] J. Xu, A. Mora, H. Shim, A. Stecenko, K. L. Brigham, M. Rojas, *American journal of respiratory cell and molecular biology* **2007**, *37* (3), 291.
[82] M. Najafi, N. Hashemi Goradel, B. Farhood, E. Salehi, M. S. Nashtaei, N. Khanlarkhani, Z. Khezri, J. Majidpoor, M. Abouzaripour, M. Habibi, *Journal of cellular biochemistry* **2019**, *120* (3), 2756.
[83] A. Heinemann, F. Zhao, S. Pechlivanis, J. Eberle, A. Steinle, S. Diederichs, D. Schadendorf, A. Paschen, *Cancer research* **2012**, *72* (2), 460.
[84] M. Kowanetz, X. Wu, J. Lee, M. Tan, T. Hagenbeek, X. Qu, L. Yu, J. Ross, N. Korsisaari, T. Cao, *Proceedings of the National Academy of Sciences* **2010**, *107* (50), 21248.
[85] W. Xu, H. Jiang, J. Gao, Y. Zhao, *Scandinavian Journal of Immunology* **2014**, *80* (1), 71.
[86] C. Cao, M. Xu, Y. Wei, T. Peng, S. Lin, X. Liu, Y. Xu, T. Chu, S. Liu, P. Wu, *Cell Genomics* **2024**, *4* (10).
[87] U. M. Domanska, R. C. Kruizinga, W. B. Nagengast, H. Timmer-Bosscha, G. Huls, E. G. de Vries, A. M. Walenkamp, *European journal of cancer* **2013**, *49* (1), 219.
[88] B. Fang, F. Ning, S. Hu, D. Guo, W. Ou, C. Wang, J. Wen, J. Sun, Z. Liu, C. A. Koh, *RSC advances* **2020**, *10* (52), 31027.
[89] A. Phan, T. Bui, E. Acosta, P. Krishnamurthy, A. Striolo, *Physical Chemistry Chemical Physics* **2016**, *18* (36), 24859.
[90] M. Z. Griffiths, W. Shinoda, *The Journal of Physical Chemistry B* **2021**, *125* (23), 6315.
[91] A. N. CALIBRATIONS, **2004**.
[92] Y. Wang, S. T. Hazeldine, J. Li, D. Oupický, *Advanced healthcare materials* **2015**, *4* (5), 729.
[93] M. C. Smith, K. E. Luker, J. R. Garbow, J. L. Prior, E. Jackson, D. Piwnica-Worms, G. D. Luker, *Cancer research* **2004**, *64* (23), 8604.
[94] S. Jo, T. Kim, V. G. Iyer, W. Im, *Journal of computational chemistry* **2008**, *29* (11), 1859.
[95] B. R. Brooks, C. L. Brooks III, A. D. Mackerell Jr, L. Nilsson, R. J. Petrella, B. Roux, Y. Won, G. Archontis, C. Bartels, S. Boresch, *Journal of computational chemistry* **2009**, *30* (10), 1545.

[96] J. Lee, X. Cheng, S. Jo, A. D. MacKerell, J. B. Klauda, W. Im, *Biophysical journal* **2016**, *110* (3), 641a.
[97] M. J. Abraham, T. Murtola, R. Schulz, S. Páll, J. C. Smith, B. Hess, E. Lindahl, *SoftwareX* **2015**, *1*, 19.
[98] A. Stukowski, *Modelling and simulation in materials science and engineering* **2009**, *18* (1), 015012.